Journal of Medicinal Chemistry

Open Access
This article is licensed under CC-BY 4.0

pubs.acs.org/jmc
Article

Development of Organocatalytic Switches of OGG1 that Protect Mitochondria under Oxidative Stress

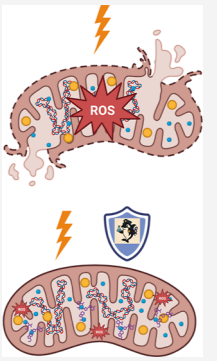
Maeve Long,* James Tribble, Rahul Upadhyay, Alice Eddershaw, Nicholas D. D'Arcy-Evans, Alan Nicol, Sara Cano, Emma Scaletti Hutchinson, Alicia del Prado, Hannah Stigsdotter, Natálie Rudolfová, Dinesh Nirmalan, Elisée Wiita, Ingrid Almlöf, Richard Svensson, Andreas Krämer, Anas Bitar, Oryn Purewal-Sidhu, Oliver Mortusewicz, Olov Wallner, Opher Gileadi, Evert J. Homan, Stefan Knapp, Pawel Baranczewski, Laurie H. Sanders, Miguel de Vega, Pål Stenmark, Alexandra Stolz, Thomas Helleday, Michael Sundström, Pete Williams, and Maurice Michel*

Cite This: J. Med. Chem. 2026, 69, 23517–23539

Read Online

ACCESS | Metrics & More | Article Recommendations | Supporting Information

ABSTRACT: Mitochondrial dysfunction is a major component of neurodegeneration. The mitochondrial genome is prone to oxidative damage, and repair proteins are important to maintain mitochondrial DNA integrity. OGG1 initiates base excision repair of oxidative DNA lesions in both nuclear and mitochondrial genomes. While inhibitors of OGG1 have been extensively explored, pharmacological activation of OGG1 through catalytic reprogramming remains underdeveloped. Herein, we report the discovery of mitochondrial enriched organocatalytic switches of OGG1. Biochemical analysis, mutational profiling, and X-ray crystallography confirmed active-site binding and preferential stimulation of β-elimination over glycosylase turnover, effectively reprogramming OGG1. We demonstrate that ORCAs protect mitochondrial function and morphology under oxidative stress, specifically affecting mitochondrial membrane potential and fragment number while attenuating metabolic stress. Mechanistically, ORCAs improved NAD levels in mouse dissociated cortical neurons and provided neuroprotection in a retina axotomy model. Together, the findings position OGG1-ORCAs as potential novel therapies for the treatment of age-related diseases and neurodegeneration.



KEYWORDS: *OGG1, organocatalytic switches, DNA glycosylase, mitochondrial function, neurodegeneration, base excision repair*

INTRODUCTION

Endogenous reactive oxygen species (ROS) arise primarily from metabolism or in response to environmental challenges and can induce oxidative DNA damage. The accumulation of oxidative DNA damage is found to be associated with various aging-related diseases including cancer and neurodegenerative disorders.[1] In DNA, guanine is vulnerable because it has the lowest redox potential among canonical DNA bases. The base is susceptible to being oxidized by ROS to generate the base lesion 8-oxo-7,8-dihydroguanine (8-oxoG), particularly at guanine-rich promoter regions.[2,3] 8-Oxoguanine DNA glycosylase 1 (OGG1) recognizes and binds 8-oxoG with high affinity in double-stranded DNA in nuclear and mitochondrial genomes to initiate base excision repair (BER), protecting cells against ROS damage.[4,5] Besides its role in BER, OGG1 has also been shown to have distinct signal transduction functions,[6,7] interact with 8-oxoG in gene regulatory regions, and facilitate gene expression specifically in inflammation.[2,7−9] Additionally, studies in mice have identified a role for OGG1 in regulating metabolism. Mitochondrial overexpression of OGG1 protects mice from obesity caused by high-fat diets, possibly through supporting the respiratory chain and oxidative phosphorylation.[10,11] In addition, upon aging, these mice are protected against neuroinflammation, indicating a protective effect mediated by OGG1.[12,13] The latter together with OGG1's role in DNA repair and gene expression regulation has sparked research in the design of small molecules targeting OGG1. Small molecule activators and inhibitors have been developed to modulate its activity in various disease models.[9,14−18] We have previously demonstrated that small molecules can enhance the activity of OGG1 by increasing DNA repair efficiency in cellular models.[14,19−21] Among them is the novel class of organocatalytic switches (ORCAs) that bind to the active site of the enzyme and stimulate the rudimentary AP lyase activity, with the ability to introduce an artificial β,δ-elimination by catalytic proton abstraction or a polarized water network.[14,16,20,22,23] With the AP lyase activity becoming dominant, the rate-determining step is removed and more OGG1 is available for 8oxoG excision in consecutive steps. This novel mechanism of action rendered OGG1 an AP lyase rather than a glycosylase, preferring AP sites over 8-oxoG.[14,20] Additional OGG1-ORCAs molecules act through different mechanisms but restore telomere and pro-

Received: February 16, 2026
Revised: September 16, 2026
Accepted: September 17, 2026
Published: October 5, 2026



ACS Publications
© 2026 The Authors. Published by American Chemical Society

https://doi.org/10.1021/acs.jmedchem.6c00526
J. Med. Chem. 2026, 69, 23517−23539

Downloaded from pubs.acs.org/jmcmar/article-pdf/69/20/23517/6749327/jm6c00526.pdf by UNIV OF SHEFFIELD user on 10 November 2026

moter integrity, alleviate inflammation, improve DNA repair, and resolve fibrosis.[14−16,24,25] However, while the apparent mode of action of OGG1-ORCAs influences transcription processes and repair in the nuclear genome,[14,15] their potential role in the mitochondria and in neurodegeneration remains underexplored.[5] In this study, we aimed to identify selective OGG1-ORCAs that rescue mitochondrial dysfunction in conditions of oxidative stress.

To initiate the search for mitochondrial selective ORCAs, we induced oxidative stress and challenged mitochondrial membrane potential (MMP) in U2OS and RPE1 cells using paraquat (PQ). We conducted an optimization campaign, monitoring improved MMP to guide and select molecules acting through the mitochondria. Through this approach, we identified a series, including **4** and **5**, that protected mitochondrial function and morphology under conditions of oxidative stress. These selective compounds act from within the active site, as corroborated by assessment against OGG1 mutants and a co-crystal structure of **4** with OGG1. The mode of action included accelerated activity on AP sites, versus 8oxoG substrates, leading to increased β-elimination, funneling OGG1 reaction products into an APE1-dependent pathway. The pharmacologically optimized compounds have demonstrated protection against oxidative stress, rescuing mitochondrial potential and morphology as well as being neuroprotective in a mouse retina axotomy model.

RESULTS

Rational Design and Synthesis of OGG1 Modulators

Previously, we developed a minimal OGG1-ORCA scaffold to assess the role of nitrogen pKa during OGG1-mediated β-elimination reactions.[16] This minimal structure (A) contained a 3,4-dichloroaniline moiety responsible for active site affinity (red in Table 1)[20] coupled in a 1,4-relationship with a pyridine ring (blue in Table 1), indeed resembling simple organic bases such as dimethyl-4-amino-pyridine (DMAP).

Building on first-generation ORCAs, our objective was not to further improve biochemical activation potency, which had already reached the low nanomolar range, but instead optimize ORCAs with improved mitochondrial activity and developability. We therefore preserved the 3,4-dichloroaniline recognition motif, previously validated by crystallography and mutational analysis to mediate productive OGG1 active-site engagement, while systematically modifying the catalytic heterocycle responsible for organocatalytic activity.[14,16,20] The optimization campaign pursued three design principles: (i) preservation of productive active-site recognition, (ii) modulation of heterocycle basicity and geometry to influence proton-transfer chemistry during β-elimination, and (iii) adjustment of physicochemical properties expected to favor mitochondrial exposure while maintaining catalytic activity.

Considering that mitochondrial exposure can be influenced by a combination of charge, lipophilicity, and molecular structure,[26] we introduced a range of heteroatoms while retaining the OGG1-binding motif. Pyrazoles, pyrrolopyridines, quinolines, and related fused bicyclic heterocycles were selected to introduce weakly basic nitrogen centers while simultaneously modulating conformational rigidity and lipophilic surface area. Calculated pKa values for the most basic sites of **4** and **5** were 5.1 and 4.9, respectively (Table S1),[27] indicating that both compounds are predominantly neutral at cytosolic pH (7.2−7.4) and mitochondrial matrix pH (~8.0). Thus, these compounds are distinct from classical permanently charged mitochondrial targeting groups, and substantial protonation-driven mitochondrial trapping is not expected. Rather, we hypothesized that incorporation of these nitrogen-containing heterocycles, together with the overall physicochemical properties of the scaffold, could improve intracellular and mitochondrial performance. We also included saturated and alternative heterocyclic ring systems (Table 1) to explore this hypothesis. Lastly, to further investigate the structure−activity relationships (SAR) within this scaffold, a focused set of analogues (10−17, Table 2) were synthesized varying the heterocyclic core and substitution pattern while retaining the 3,4-dichloroaniline moiety.

Scheme 1 explores electronic effects on the aniline recognition motif while maintaining an invariant catalytic scaffold. The synthesis of the compounds (Scheme 1, **4** and **10**−**15**) was conducted *via* nucleophilic aromatic substitution between the chloro-substituted pyrazolo compound (a) and various substituted anilines (b) in the presence of trifluoroacetic acid in 2,2,2-trifluoroethanol at 80 °C for 16 h. The reaction afforded the desired products in moderate to good yields (22−80%). Anilines bearing electron-withdrawing substituents generally provided higher yields compared with unsubstituted or electron-donating substituted anilines.

Scheme 2 investigates alternative fused heterocyclic cores to probe how ring fusion, heteroatom placement, and scaffold rigidity influence catalytic enhancement. By using the same nucleophilic substitution reaction, we further explore the reaction of 3,4-dichloroaniline with different chloro-substituted heterocyclic scaffolds such as thieno-pyridine, quinoline, dihydro-cyclopenta-pyridine, pyrrolo-pyridine, and pyrazolo-pyrimidine. The reactions resulted in moderate to good yields of the desired compounds, as shown in Scheme 2 (**1**−**3**, **16**, **17**). This strategy enabled the rapid generation of structurally diverse analogues for further evaluation. However, for 4-chloro-6,7-dihydro-5*H*-cyclopenta[*b*]pyridine, the coupling with aniline derivatives was achieved using a palladium-catalyzed amination reaction, affording the desired product (**6**) in moderate yield.

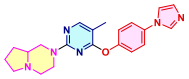
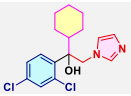
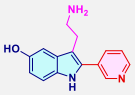
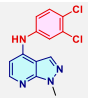
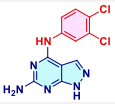
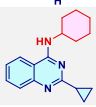
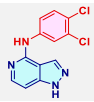
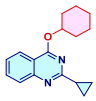
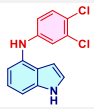
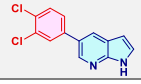
Scheme 3 introduces more disruptive modifications designed to probe the importance of nucleophile orientation and active-site geometry for productive catalysis. To further explore the SAR, a series of structurally diverse molecules were synthesized (Scheme 3). The selective pyrazolo *N*-alkylation was accomplished by reacting compound **4** (a) with methyl iodide (b) in the presence of Cs_2CO_3, which afforded the *N*-methylated product **5** in 60% yield. In a parallel approach, 4-chloro-1*H*-pyrazolo[4,3-*c*]pyridine (a) underwent nucleophilic aromatic substitution with 2,4-dichloroaniline (b) under neat conditions at 100 °C for 24 hours to give compound **7** in 55% yield. Additionally, the Buchwald−Hartwig amination of 4-bromo-1,2-dichlorobenzene (a) with 1*H*-indol-4-amine (b) led to the formation of compound **8** in 36% yield, while a Suzuki−Miyaura cross-coupling of 5-bromo-1*H*-pyrrolo[2,3-*b*]pyridine (a) with (3,4-dichlorophenyl)boronic acid (b) using $Pd(dppf)Cl_2$ smoothly produced compound **9** in 74% yield.

We then determined the AC_{50}—the concentration of the compounds inducing 50% AP lyase activity compared to APE1—using an established fluorophore−quencher pair-based assay.[14] Except for the methylated pyrazole derivative **5** (364 nM), the reintroduction of a second ring did not affect the activity of the molecules, and high potency was retained within the series ranging from 9 to 120 nM (Tables 1 and 2).

Downloaded from pubs.acs.org/jmcmar/article-pdf/69/20/23517/6749327/jm6c00526.pdf by UNIV OF SHEFFIELD user on 10 November 2026

https://doi.org/10.1021/acs.jmedchem.6c00526
J. Med. Chem. 2026, 69, 23517−23539

Table 1. Previously Generated Molecules Targeting OGG1 and Putative OGG1-ORCAs Generated in This Study[a]

Compound #	Structure	AC_{50} (CI95%) [μM]	Compound #	Structure	AC_{50} (CI95%) [μM]
A[16]		0.013 (0.010-0.016)	**1**		0.034 (0.029-0.039)
B[21]		EC_{50} 4.6	**2**		0.010 (0.006-0.017)
C[21]		EC_{50} 5.0	**3**		0.018 (0.005-0.069)
D[16]		0.100 (0.080–0.120)	**4**		0.029 (0.018-0.048)
E[23]		0.58 (0.37-0.92)	**5**		0.364 (0.316-0.419)
F[20]		13.1 (2.3-75.1)	**6**		0.017 (0.006-0.047)
TH10785[14]		0.87 (0.70-1.1)	**7**		inactive
TH11738[14]		inactive	**8**		inactive
			9		2.92 (0.75-4.14)

[a]Left column contains compounds known in the literature. Right column describes compounds made in this study. AC_{50}—50% activation of compound with OGG1 compared to OGG1 and APE1. CI95%—confidence intervals 95%. EC_{50}—50% of the maximum stimulatory effect on OGG1. Results of three independent experiments.

Despite considerable structural variation, most analogues retained low nanomolar activation potency, indicating that productive organocatalytic enhancement is remarkably tolerant to modification provided that the active-site recognition motif is preserved. Electron-withdrawing and electron-donating substituents on the aniline ring had only modest effects on activity, consistent with this region primarily contributing to binding rather than catalysis. In contrast, alterations to the catalytic heterocycle modulated activity to a greater extent, suggesting that heterocycle electronics and geometry influence the proton-transfer events underlying β-elimination. Importantly, biochemical potency rapidly plateaued across the series, indicating that further optimization should primarily focus on cellular and physicochemical properties rather than equilibrium binding affinity.

Discovery of OGG1 Modulators that Rescue Mitochondrial Membrane Potential

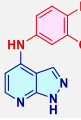
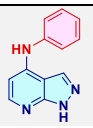
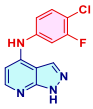
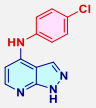
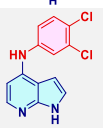
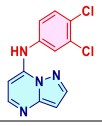
As the next step, we set up a live cell microscopy-based screening method in U2OS to identify analogues that can rescue the MMP following treatment with PQ, which induces oxidative stress and mitochondrial dysfunction.[28] Mechanistically, PQ cycles redox equivalents within the mitochondria, producing ROS primarily at Complex I of the respiratory chain, reducing NAD levels as a result.[29] Briefly, U2OS cells were seeded in 96-well plates and treated with the control (DMSO) or PQ for 24 h alone or in combination with 1 μM or 10 μM compounds **B** and **C** (Table 1), previously reported to affect the MMP.[19,21] Following 24 h of treatment, cells were incubated with tetramethylrhodamine, methyl ester, and perchlorate (TMRM), a cell-permeable cationic, red-orange, fluorescent dye that is sequestered by active mitochondria with a functional MMP. Mitochondria with damaged MMP have lower dye retention and hence lower intensity of the dye in the mitochondria. MMP and cell confluency were measured in each well by live cell microscopy on a Spark Cyto (Figures 1A and S1).

The use of the redox cycler PQ caused a decrease in mitochondrial membrane potential at a concentration of 0.6 mM without an effect on cell viability after 24 h (Figures 1B,C and S1). To confirm the usefulness of the approach, we applied OGG1 modulators **B** and **C**, which influence the MMP in a positive and negative manner, respectively (Figure 1B,C).[19] **B** had no effect on cell confluency, while **C** caused cell viability loss at higher concentrations (Figure S1). Using this setup, we screened a representative set of OGG1-ORCAs (**1**–**6**), including previously generated legacy compounds (**A**–**F**, TH10785, and TH11738, Table 1).[16,20,23] In this screen, we identified novel compounds **4** and **5** that rescued MMP under conditions of oxidative stress when used at 10 μM (Figure 1D). Compound **2**, the most potent analogue of the series in vitro,

Downloaded from pubs.acs.org/jmcmar/article-pdf/69/20/23517/6749327/jm6c00526.pdf by UNIV OF SHEFFIELD user on 10 November 2026

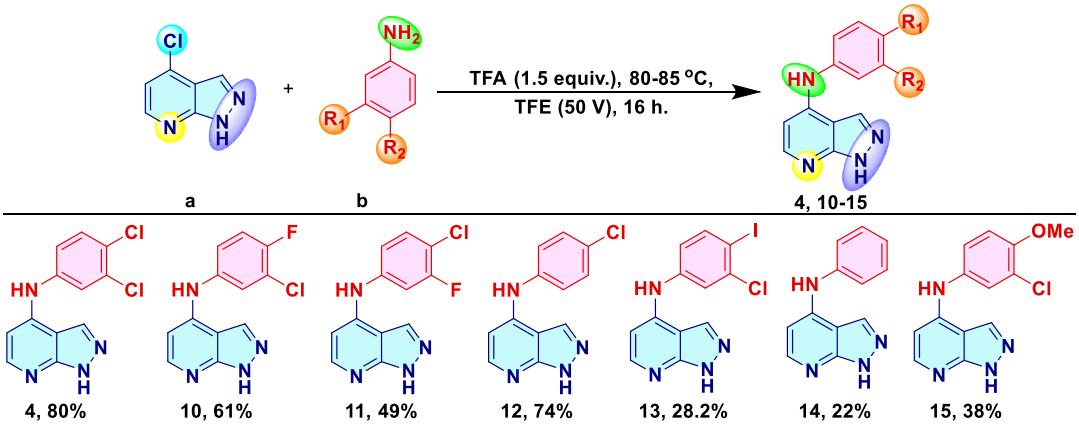
https://doi.org/10.1021/acs.jmedchem.6c00526
J. Med. Chem. 2026, 69, 23517–23539

Table 2. Structural Changes Introduced to the Scaffold of 4 and 5, Generating Putative OGG1-ORCAs[a]

Compound #	Structure	AC_{50} (CI95%) [μM]	Compound #	Structure	AC_{50} (CI95%) [μM]
10		0.063 (0.028-0.139)	**14**		0.061 (0.031-0.118)
11		0.019 (0.002-0.215)	**15**		0.021 (0.002-0.171)
12		0.061 (0.009-0.430)	**16**		0.009 (0.008-0.010)
13		0.033 (0.004-0.255)	**17**		0.120 (0.049-0.296)

[a]AC_{50}—50% activation of the compound with OGG1 compared to OGG1 and APE1. CI95%—confidence intervals 95%. EC_{50}—50% of the maximum effect on OGG1. Results of three independent experiments.

Scheme 1. Synthetic Route of Compounds 4 and 10−15[a]



[a]Reaction conditions: 4-chloro-1*H*-pyrazolo[3,4-*b*]pyridine a (1.0 equiv.), aniline derivatives b (1.1 equiv.), 2,2,2-trifluoroethanol (50 V), 80-85 °C, 16 h. Yields: Isolated yield.

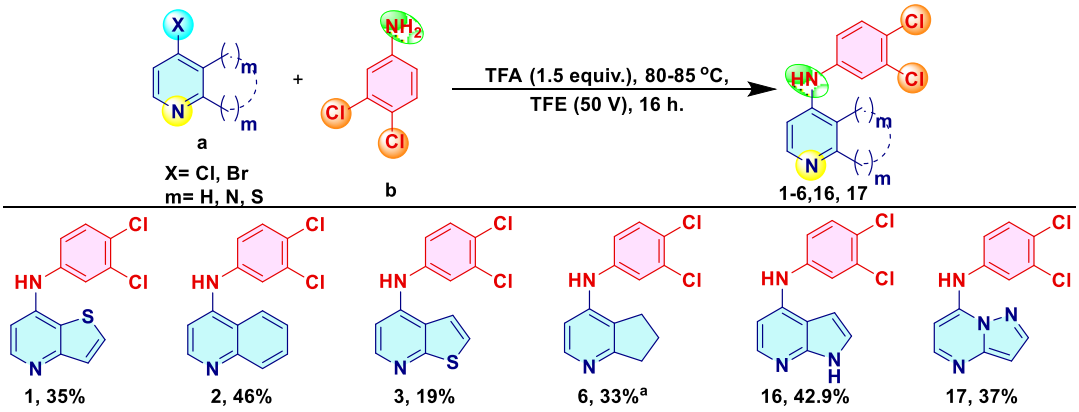
also rescued the MMP, albeit to a lower level, and was the only active compound not bearing an additional nitrogen center. Several molecules were identified that worsened MMP or were ineffective in cells treated with PQ, among them compounds of the series of **A**[16] and the recently reported serotonin derivative **E**.[23] Of the newly synthesized compounds **A**−**F**, none effected a change in cell confluency (Figure S1C).[19,21]

To corroborate that a boosting of OGG1 activity was responsible for the improvements in MMP, we had generated several negative control compounds above. This included migration (**7**) or deletion of the active nitrogen (**8**), as well as moving the 3,4-dichloro-phenyl substitution (**9**). While **9** retained some activity (albeit 100-fold less compared to **4**), **7** and **8** were shown to be entirely inactive in the biochemical assay (Table 1), with **7** confirming this result in the readout for MMP (Figure S2). We next carried out dose response curves in the MMP and cell confluency assay with the newly identified ORCAs **4**, **5**, the negative control **7**, and compound **B** (Figure S2A). Once again, compounds **4** and **5** were found to rescue MMP similarly to **B**, while the negative control **7** had no effect on MMP (Figure S2A). For **5** and **7**, a negative effect on cell confluency was noted at 30 μM, while no effect was seen for the other compounds at these concentrations (Figure S2B). Collectively, these cellular SAR data suggest that incorporation of the additional nitrogen-containing heterocycle is associated with improved mitochondrial activity within this compound series as compounds **4** and **5** showed pronounced rescue of MMP, whereas structurally related analogues lacking or repositioning this feature were less effective or inactive. Compound **2** represents an exception, displaying a weaker MMP rescue despite lacking the additional nitrogen center. Thus, the nitrogen-containing heterocycle appears beneficial, but not strictly required, for the mitochondrial phenotype and should be considered together with the overall physicochemical properties of

Downloaded from pubs.acs.org/jmcmar/article-pdf/69/20/23517/6749327/jm6c00526.pdf by UNIV OF SHEFFIELD user on 10 November 2026

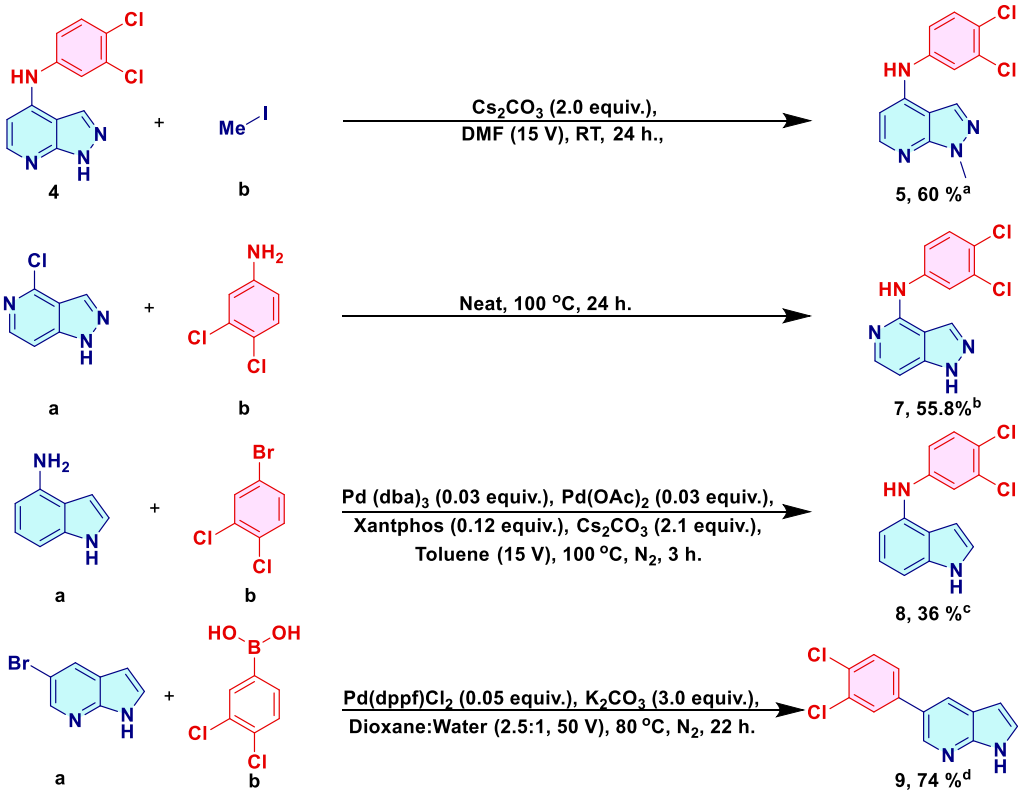
https://doi.org/10.1021/acs.jmedchem.6c00526
J. Med. Chem. 2026, 69, 23517−23539

Scheme 2. Synthetic Route of Compounds 1−6, 16, and 17[a]



[a]Reaction conditions: Halo-compound a (1.0 equiv.), 3,4-dichloroaniline b (1.1 equiv.), 2,2,2-trifluoroethanol (50 V), 80−85 °C, 16 h. [a]4-chloro-6,7-dihydro-5*H*-cyclopenta[*b*]pyridine a (1.0 equiv.), 3,4-dichloroaniline b (1.15 equiv.), sodium tert-butoxide (1.23 equiv.), $Pd(dba)_2$ (4 mol %), JohnPhos (7 mol %) toluene (30 V), N_2, 85 °C, 3 days. Yields: Isolated yield.

Scheme 3. Synthetic Route of Compounds 5 and 7−9[a]



[a]Reaction conditions: [(a)]*N*-(3,4-dichlorophenyl)-1*H*-pyrazolo[3,4-*b*]pyridin-4-amine **4** (1.0 equiv.), iodomethane b (1.3 equiv.), DMF (15 V), RT, 24 h. [(b)]4-chloro-*1H*-pyrazolo[4,3-*c*]pyridine a (1.0 equiv.), 3,4-dichloroaniline b (1.1 equiv.), 100 °C, 24 h. [(c)]4-chloro-6,7-dihydro-5*H*-cyclopenta[*b*]pyridine a (1.0 equiv.), 3,4-dichloroaniline b (1.15 equiv.), sodium tert-butoxide (1.23 equiv.), $Pd(dba)_2$ (4 mol %), JohnPhos (7 mol %) toluene (30 V), N_2, 85 °C, 3 days. Yields: Isolated yield. [(d)]5-bromo-1*H*-pyrrolo[2,3-*b*]pyridine a (1.0 equiv), (3,4-dichlorophenyl)boronic acid b (1.2 equiv.), $Pd(dppf)Cl_2$ (5 mol %), potassium carbonate (3.0 equiv.) in dioxane:water (5 mL {2.5:1}), N_2, 80 °C, 22 h.

the scaffold rather than as a discrete mitochondrial targeting group.

Mitochondrial OGG1 Modulators Enhance the OGG1 AP Lyase Activity from within the Active Site

We next assessed the molecular properties and mode of action of **4** and **5**. ORCAs are known to selectively exhibit their effect from within the active site of OGG1, while the enzyme is bound to the Schiff-base intermediate that results from base excision. As such, the compounds may compete with or inhibit the glycosylase function of OGG1, where their binding is non-productive, leading to a bell-shaped curve activity profile due to the interconnectivity of both enzymatic activities of OGG1.[14,20] To determine if **4** preferably stimulated the inherent but weak AP lyase activity of OGG1, we performed biochemical experiments titrating the compound against sub-saturating and

Downloaded from pubs.acs.org/jmcmar/article-pdf/69/20/23517/6749327/jm6c00526.pdf by UNIV OF SHEFFIELD user on 10 November 2026

https://doi.org/10.1021/acs.jmedchem.6c00526
J. Med. Chem. 2026, 69, 23517−23539

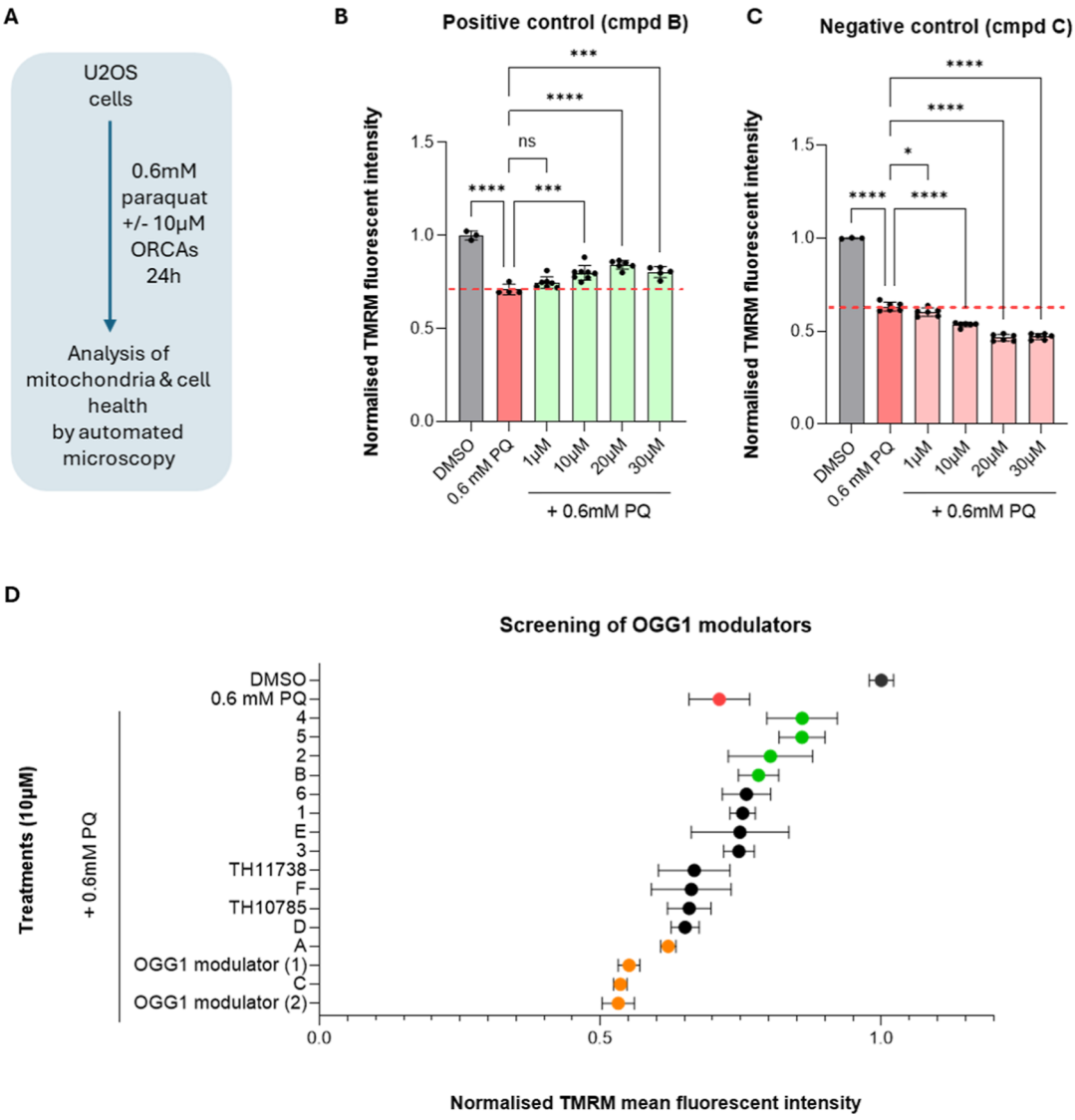


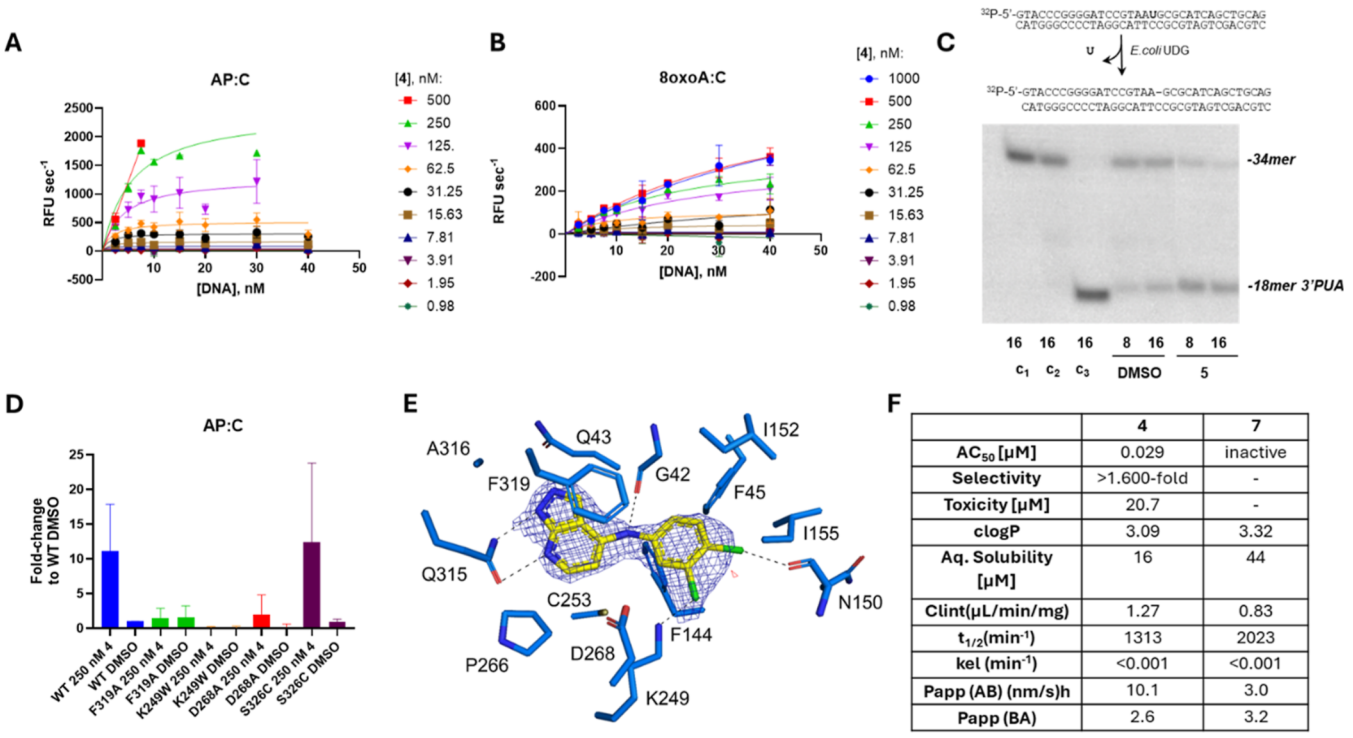
Figure 1. Screen with a set of OGG1 modulators identifies small molecules that rescue mitochondrial membrane potential under the condition of oxidative stress. (A) Diagram depicting the screen setup and workflow. U2OS cells were seeded in 96-well plates and treated with the control (DMSO) or PMitochondrial membrane potential was analyzed using TMRM and automated microscopy. Cell confluency was also measured simultaneously. (B) A previously characterized OGG1 activator[19,21] was used to rescue the MMP following paraquat treatment in a concentration-dependent manner. Data from three independent experiments are displayed as means ± SD, $n = 3$. (C) A previously characterized OGG1 activator[19,21] was used to worsen the MMP following paraquat treatment in a concentration-dependent manner. Data from three independent experiments are displayed as means ± SD, $n = 3$. (D) Screen for OGG1 modulators that can rescue the loss of MMP following paraquat treatment. Compounds that rescue MMP significantly are color coded in green, while those that significantly worsen MMP are color coded in orange. Data from three independent experiments are displayed as means ± SD, $n = 3$. ****$P < 0.0001$, ***$P < 0.001$.

saturating concentrations of DNA substrates containing either an AP site opposite cytosine (Figure 2A) or 8-oxoA opposite cytosine (Figure 2B). For the 8-oxoA substrate, a more stable substrate than 8-oxoG,[20] no bell-shaped curve was observed at concentrations up to 1 μM, indicating selectivity of the compound for the OGG1−Schiff-Base complex over apo OGG1. With the AP/C substrate, fluorescent signals reached saturating conditions for the plate reader at the top DNA concentrations when **4** was above 0.5 μM. We observed on average a 12-fold increase in incision rate of the AP site at 250 nM **4** (Figure 2D) when the substrate was equimolar to enzyme (10 nM), as well as activity of the compound below the concentration of the protein (Figure 2A).

Previously, we demonstrated that OGG1 may also catalyze an artificial δ-elimination in addition to the canonical β-elimination (AP lyase). To determine if structures of type **4** convey a new-found activity, we performed PAGE using radioactively labeled DNA strands (Figure 2C). As observed previously, OGG1 alone showed low efficacy in incising the DNA backbone. For **5**, the methyl analogue of **4**, we observed an improved catalysis of OGG1 on AP sites. Rapid formation of 3′-phospho-α,β-unsaturated-aldehyde (3′-PUA) indicated an efficient β-elimination taking place. This confirms that the present chemical series renders OGG1 an efficient AP lyase, creating a product that is amenable to derivatization by APE1, the canonical initiation of BER.

Downloaded from pubs.acs.org/jmcmar/article-pdf/69/20/23517/6749327/jm6c00526.pdf by UNIV OF SHEFFIELD user on 10 November 2026

https://doi.org/10.1021/acs.jmedchem.6c00526
J. Med. Chem. 2026, 69, 23517−23539



F

	4	7
AC_{50} [μM]	0.029	inactive
Selectivity	>1.600-fold	-
Toxicity [μM]	20.7	-
clogP	3.09	3.32
Aq. Solubility [μM]	16	44
Clint(μL/min/mg)	1.27	0.83
$t_{1/2}$(min^{-1})	1313	2023
kel (min^{-1})	<0.001	<0.001
Papp (AB) (nm/s)h	10.1	3.0
Papp (BA)	2.6	3.2

Figure 2. 4 is an ORCA with favorable physicochemical properties. (A,B): Effect of **4** on the rate of DNA incision: Initial slope measured in the standard fluorophore−quencher assay using either the AP:C (A) or 8oxoA:C (B) DNA substrate at indicated concentrations in the presence of 10 nM hOGG1 and **4** at indicated concentrations. AP sites were generated from the U:C substrate using UDG. (C) On the top, schematics of the [^{32}P]5′-labeled 2′deoxyuridine-containing DNA substrate used during the reaction. 1 nM concentration of the DNA substrate, previously treated with 0.2 U of UDG to obtain a natural AP site, was incubated with 75 nM hOGG1 and either 10% DMSO or 6.25 μM **5** as indicated. After incubation for the indicated times at 37 °C, reactions were stopped, and the products were resolved by 7 M urea-20% PAGE and visualized by autoradiography. Position of products is indicated. C_1: DNA control not pretreated with UDG; C_2: Control of UDG-pretreated DNA; C_3: Alkalyne hydrolysis of AP sites. (D) Assessment of wt and mutant OGG1 activation by **4**. Initial rates measured in the standard fluorophore−quencher assay using a 10 nM AP:C substrate, 10 nM wt, F319A, K249 W, or D268A hOGG1 or 20 nM S326C hOGG1 and 0.25 μM **4**; Δ RFU s^{-1} = change of relative fluorescence units per second. (E) The recognition of ligand **4** (PDB ID: 9GIH) by mOGG1. Amino acids contributing to ligand binding are depicted as sticks: C atoms are colored blue, O atoms are colored red, and N atoms are colored dark blue. The ligands are depicted as a stick model: C atoms are colored yellow, N atoms are colored dark blue, and Cl are colored green. Hydrogen and halogen bond interactions are shown as dashed lines. The 2Fo-Fc electron density maps around **4** are contoured at 1.0 σ (blue), and the Fo-Fc electron density maps are contoured at +3.5 s (green) and −3.5 s (red). Figure produced using PyMOL (v.2.3.3, Schrödinger). (F) Physicochemical Properties of **4** and **7**: AC_{50} as in Table 1. Selectivity: Calculated as the lowest IC_{50} measured against a panel of DNA glycosylases and NUDIX nucleotide binding proteins/OGG1 AC_{50}. Toxicity: Incubation in BJ-RAS and BJ-TERT cell lines. Kinetic solubility in PBS buffer (pH 7.4). Metabolic stability evaluated in human liver microsomes. Permeability AB/BA: Using the Caco-2 cell line.

To qualify as ORCAs, the compounds needed to bind the active site while assisting in catalysis through OGG1. To investigate whether **4** was indeed bound to the catalytic center of OGG1 during catalysis, we used a range of OGG1 variants and assessed their amenability to enhancement by **4**. The amino acids variants Phe319Ala, Cys253Tyr ,and Lys249Trp within the active site were not affected by the presence of the compound. The OGG1 protein mutated at the active site residue responsible for stabilizing the AP site, Asp268Ala,[30] and the human variant Ser326Cys[31] located about 4−5 Ångström from the active site were markedly enhanced by compound **4** (Figure 2D). These data indicated that active site mutation occluded the compound, while variations of canonical amino acids placed sufficiently far away or involved in catalysis were not interfering with compound binding.

To corroborate this finding and to determine the binding mode of **4**, we determined the X-ray crystal structure of mouse OGG1 in complex with the ligand to 2.27 Å resolution (Table S2). Clear electron density for **4** was observed in the active site (Figure 2E), with binding overlapping with the previously reported ORCA TH10785 (Figure S3). Mouse and human OGG1 share conserved active-site residues, with the mouse enzyme being more amenable to crystallization. Consistent with conservation of an organocatalytic mechanism, compound **4** enhanced AP lyase activity of both enzymes, although a quantitative species-dependent difference in potency was observed, with AC_{50} values of 0.026 μM for hOGG1 and 0.30 μM for mOGG1 (95% CI 0.16−0.51 μM). **4** is positioned by H−bonds between the fused heterocyclic ring and Gln315 and the secondary amine linker and the backbone oxygen of Gly42, as well as H−bonds between the dichlorobenzene ring and the sidechain of Lys249 and a halogen bond to the oxygen of Asn150. Furthermore, **4** binding is supported by a π-stacking interaction with Phe319, in addition to extensive hydrophobic interactions involving Gln43, Phe45, Phe144, Ile152, Ile155, Cys253, Met257, Pro266, Asp268, and Ala316 (Figure 2E), overall complementing the mutational studies in Figure 2D. Together, the data support that the identified compounds bind the active site for catalysis, rendering them organocatalytic switches.

Downloaded from pubs.acs.org/jmcmar/article-pdf/69/20/23517/6749327/jm6c00526.pdf by UNIV OF SHEFFIELD user on 10 November 2026

https://doi.org/10.1021/acs.jmedchem.6c00526
J. Med. Chem. 2026, 69, 23517−23539

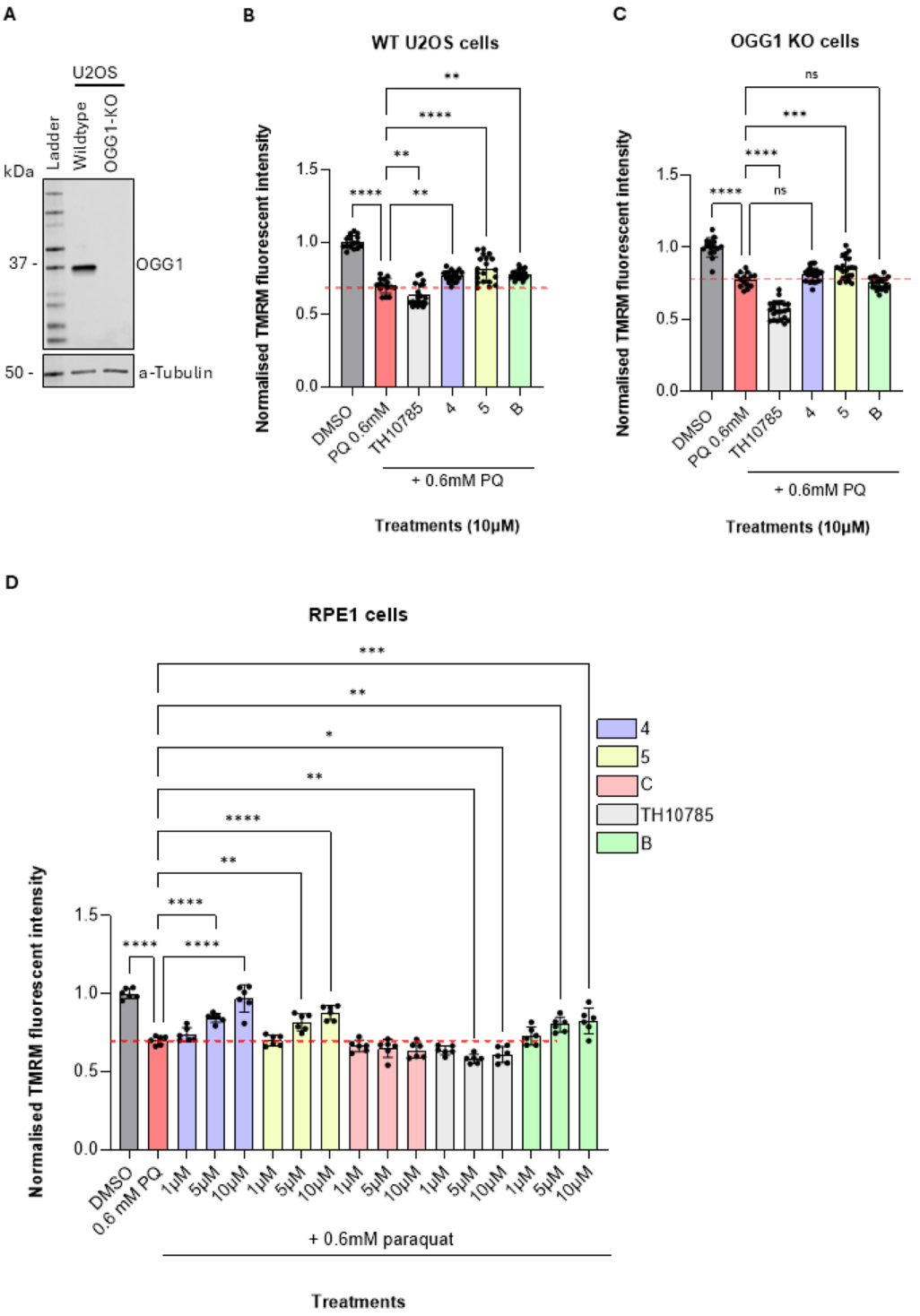


Figure 3. Compound **4** is a novel OGG1-ORCA that rescues MMP in oxidative stress conditions through OGG1. (A) Western blot showing OGG1 knockout in U2OS cells by CRISPR cas9. (B,C) U2OS ORCAs were tested for OGG1 specificity using wild-type U2OS cells and OGG1 knockout cells. U2OS cells were treated with a control (DMSO) or paraquat w/o OGG1 ORCAs for 24 h, and MMP was measured by TMRM staining and analyzed by automated microscopy. Data from three independent experiments are displayed as mean ± SD, $n = 3$. (D) RPE1 cells were treated with a control (DMSO) or paraquat w/o OGG1-ORCAs for 24 h, and MMP was measured by TMRM staining and analyzed by automated microscopy. Data from three independent experiments are displayed as the mean ± SD, $n = 3$. $^{****}P < 0.0001$, $^{***}P < 0.001$, $^{**}P < 0.005$.

Mito-ORCAs Are Selective for OGG1 and Exhibit a Favorable Physicochemical In Vitro Profile

To further determine whether **4** and **5** acted through OGG1 while rescuing the MMP, we evaluated compound specificity using OGG1 knockout U2OS cells generated by CRIPSR Cas9 (Figure 3A−C). In the OGG1 knockout cells, **4** no longer rescued MMP in conditions of oxidative stress (Figure 3C) compared to the rescue in WT OGG1 cells (Figure 3B). In contrast, **5** retained partial MMP rescue in OGG1 KO cells, demonstrating an OGG1-independent component to its cellular

Downloaded from pubs.acs.org/jmcmar/article-pdf/69/20/23517/6749327/jm6c00526.pdf by UNIV OF SHEFFIELD user on 10 November 2026

https://doi.org/10.1021/acs.jmedchem.6c00526
J. Med. Chem. 2026, 69, 23517−23539

activity. This genetic differentiation between the closely related analogues **4** and **5** was important for compound prioritization. Despite retaining biochemical ORCA activity, the *N*-methylated analogue **5** showed reduced mechanistic selectivity at the cellular level, whereas the MMP-rescue activity of **4** was dependent on OGG1. Compound **4** was therefore prioritized for subsequent mechanistic and mitochondrial characterization. The molecular target responsible for the residual OGG1-independent activity of **5** remains unknown and was not investigated further in this study. At the same time, compound **B** was selective for OGG1 as no rescue was shown in OGG1 KO cells compared to WT cells (Figure 3B−C). As U2OS cells are transformed cancer cells, we also tested the ORCAs in RPE1 cells, which are an immortalized line of human retinal pigment epithelial cells. In these cells, **4**, **5**, and **B** caused a dose-dependent rescue of MMP, with complete recovery of the MMP at 10 μM (Figure 3D), surpassing the effect in U2OS cells. No effect on cell confluency was detected (Figure S4), indicating the non-toxic behavior of the compounds. Furthermore, as compound **4** exhibits MMP rescue through OGG1 and given OGG1 localization to mitochondria,[4] we carried out experiments with the aim of verifying mitochondrial enrichment of compound **4**. Using mitochondrial isolation followed by LC/MS, we show that compound **4** is enriched in mitochondria (Figure S5). RPE1 cells were treated with 20 μM compound **4** or DMSO for 2 h prior to mitochondrial isolation. Western blotting experiments of mitochondrial proteins (outer-membrane mitochondrial protein TOMM20 and inner-membrane mitochondrial protein COX IV) and nuclear proteins (Lamin A/C and Histone H3) (Figure S5A) show enrichment of mitochondrial and not nuclear proteins in mitochondrial fraction 2 in each biological replicate. Fraction 2 was then processed for LC/MS and analysis revealed the presence of compound **4** in these fractions, indicating enrichment of compound **4** in isolated mitochondria of RPE1 cells (Figure S5B). The calculated pKa of the most basic site of **4** was 5.1, corresponding to only a minor protonated fraction at cytosolic pH (7.2−7.4) and an even lower fraction at the more alkaline mitochondrial matrix pH (∼8.0). Compound **4** is therefore expected to remain predominantly neutral under both conditions, arguing against classical pH-dependent ion trapping as the principal explanation for its mitochondrial enrichment. Instead, the observed enrichment likely reflects the combined physicochemical properties of the scaffold, including its weakly basic heterocycle and lipophilic character (clogP 3.09), although the precise mechanism of mitochondrial accumulation remains to be established.

To further study potential cytotoxicity of **4**, we then exposed BJ-TERT cells derived from a human fibroblast cell line that has been immortalized by the introduction of the human telomerase reverse transcriptase (h-TERT) and BJ-Ras cells, which are driven by the expression of the oncogene Ras, to increasing doses of compounds of the series (Table S3). No difference between the two cell lines was observed, with EC_{50} found between 20 and 30 μM, indicating no toxicity at the concentrations used. In the following, we assessed whether the identified compounds bind alternative targets and performed selectivity screens against other DNA glycosylases and NUDIX protein members as proteins that commonly bind nucleobase and derivatives thereof (Table S4). We observed no inhibition at the relevant concentration, with partial inhibition at 100 μM for TDG, UNG2, SMUG1. and NUDT22. Due to the resemblance of a hinge binding motif, we further evaluated **4** and the negative control **7** in a screen against a representative set of 94 kinases plus 5 usual kinase off targets, testing thermal stability using differential scanning fluorimetry (DSF, Table S5). **4** was found to be overall selective and the negative control **7** stabilized a few kinases not known to interact with OGG1 biology. With ORCA **4** shown to be selective and non-toxic at used concentrations, we then determined in vitro physicochemical properties (Figure 2F). In addition to the observed high selectivity and low toxicity levels, the compound exhibited a favorable clogP of 3.09 with a solubility of 16 μM. In addition, the measured clearance, half-life, elimination rate, and permeability were excellent. These experiments indicate that the pyrazole analogue **4** is a selective, non-toxic, and physiochemically favorable modulator of OGG1.

Mito-ORCAs Rescue Mitochondrial Morphology under Oxidative Stress

Since **4** was the most specific compound among those tested against OGG1 using the OGG1 KO cells, we focused on its role in mitochondria in greater detail. Mitochondrial morphology is negatively affected by oxidative stress. To determine whether **4** alleviated this impact, we next analyzed mitochondria morphology in response to oxidative stress using confocal microscopy and cells stained with Translocase of Outer Mitochondrial Membrane 20 (TOMM20). PQ treatment caused an increase in mitochondrial fragment number per cell compared to control (DMSO)-treated cells (Figure 4A−B). The exposure to **4** caused a decrease in mitochondrial fragments to levels comparable to fragment number in control (DMSO)-treated cells. Importantly, TH10785 did not affect the mitochondrial number, highlighting the need to apply mitochondrial selective and specific ORCAs. Additionally, we next used super-resolution microscopy and cells stained with the mitochondrial marker transcription factor A (mt-TFA) and TOMM20 to confirm these results, showing that **4** rescued mitochondria morphology in conditions of oxidative stress to levels of mitochondrial fragmentation comparable to those found in control (DMSO)-treated cells (Figure 4C−D).

Fragmentation of the mitochondrial network and mitochondrial dysfunction are both linked to increased oxidative stress. Therefore, we assessed whether **4** affected ROS levels in cells. U2OS cells were first pretreated with menadione for 1 h, followed by cell washout and incubation with TH10785 or **4** for 1 h. Cellular ROS was then measured using the live cell dye CellROX by confocal microscopy (Figure 4D). **4** but not TH10785 caused a reduction in cellular ROS to levels comparable to those found in control (DMSO)-treated cells, confirming that improving OGG1 activity within the mitochondria directly influences cellular ROS levels. In addition, OGG1 is localized to mitochondria where it has a role in DNA repair.[4] Using Mito DNA_{DX}, a PCR-based assay that allows for the accurate real-time quantification of mtDNA damage, as previously described in Qi et al.,[32] we demonstrate that compound **4** decreases mtDNA damage levels following paraquat treatment (Figure S6A). These data support emerging evidence that targeting the mitochondria is a viable approach to counteract excessive amounts of ROS.[31]

Mito-ORCAs Rescue NAD^+ Levels and Protect Neurons against Axotomy-Induced Degeneration

Since overexpression of mitochondrial OGG1 was previously shown to affect bioenergetics and oxidative phosphorylation[11,12] and considering that PQ depletes Nicotinamide Adenine Dinucleotide (NAD) levels in a cell,[34] we argued that targeting the mitochondria with OGG1-ORCAs may positively affect NAD levels. To determine such an influence, we performed targeted

Downloaded from pubs.acs.org/jmcmar/article-pdf/69/20/23517/6749327/jm6c00526.pdf by UNIV OF SHEFFIELD user on 10 November 2026

https://doi.org/10.1021/acs.jmedchem.6c00526
J. Med. Chem. 2026, 69, 23517−23539

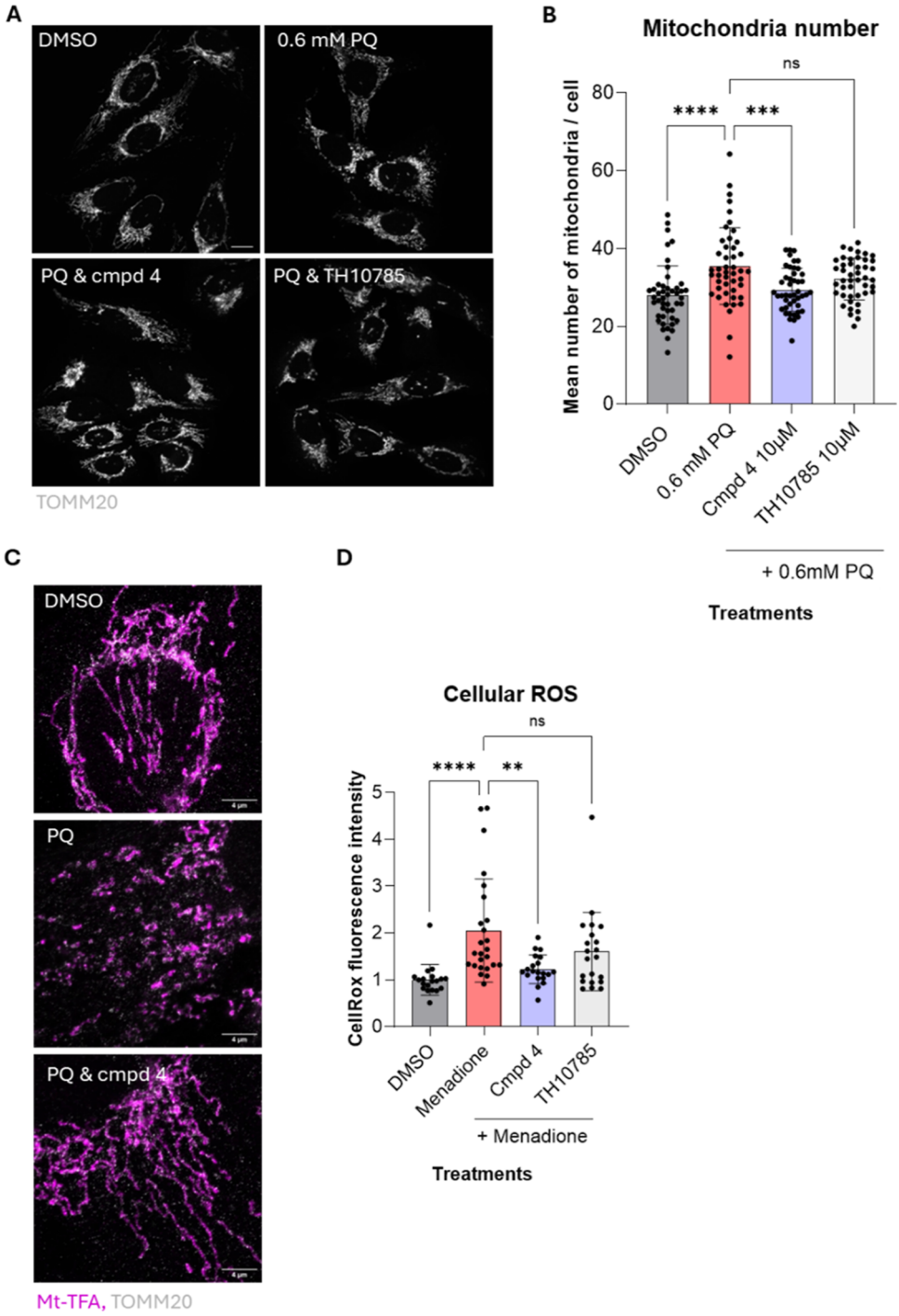


Figure 4. Compound **4** rescues mitochondrial morphology under oxidative stress conditions. (A) U2OS cells were treated with the control (DMSO), 0.6 mM PQ, or 0.6 mM PQ in combination with compound **4** or TH10785 for 24 h. Cells were then fixed and stained for mitochondria using mt-TFA and nucleus with Hoechst33342. (B) Cells were imaged on a confocal microscope, and images were analyzed with CellProfiler. A graph representing the mean number of mitochondrial fragments per cell is displayed. Data from three independent experiments are displayed as means ± SD, $n = 3$. (C) Super-resolution microscopy was carried out on U2OS cells stained with mt-TFA and TOMM20 treated in the same way as in (A). (D) U2OS cells were treated with the control (DMSO) or 100 μM menadione for 1 h. Cells were then allowed to recover in media or media containing 10 μM **4** or 10 μM TH10785 for 1 h. Cells were incubated with CellROX dye and live-cell imaged on a confocal microscope. Fluorescent intensity of CellROX was analyzed, and results are displayed on a graph. Data from three independent experiments are shown as means ± SD, $n = 3$. $^{****}P < 0.0001$, $^{***}P < 0.001$, $^{**}P < 0.005$.

NAD assays. Dissociated cortex was incubated with **4**, **5**, and **B** at 1 μM and 10 μM for 2 h (Figure 5A,B). All compounds significantly increased NAD at 10 μM compared to the vehicle (DMSO)-treated cortex, with **4** demonstrating the largest NAD increase (Figure 5B). The increase in NAD demonstrated by these compounds may offer a potential direct mechanism by which these compounds provide neuroprotection (i.e., increased NAD:NMN ratios slowing Wallerian degeneration).

Downloaded from pubs.acs.org/jmcmar/article-pdf/69/20/23517/6749327/jm6c00526.pdf by UNIV OF SHEFFIELD user on 10 November 2026

https://doi.org/10.1021/acs.jmedchem.6c00526
J. Med. Chem. 2026, 69, 23517–23539

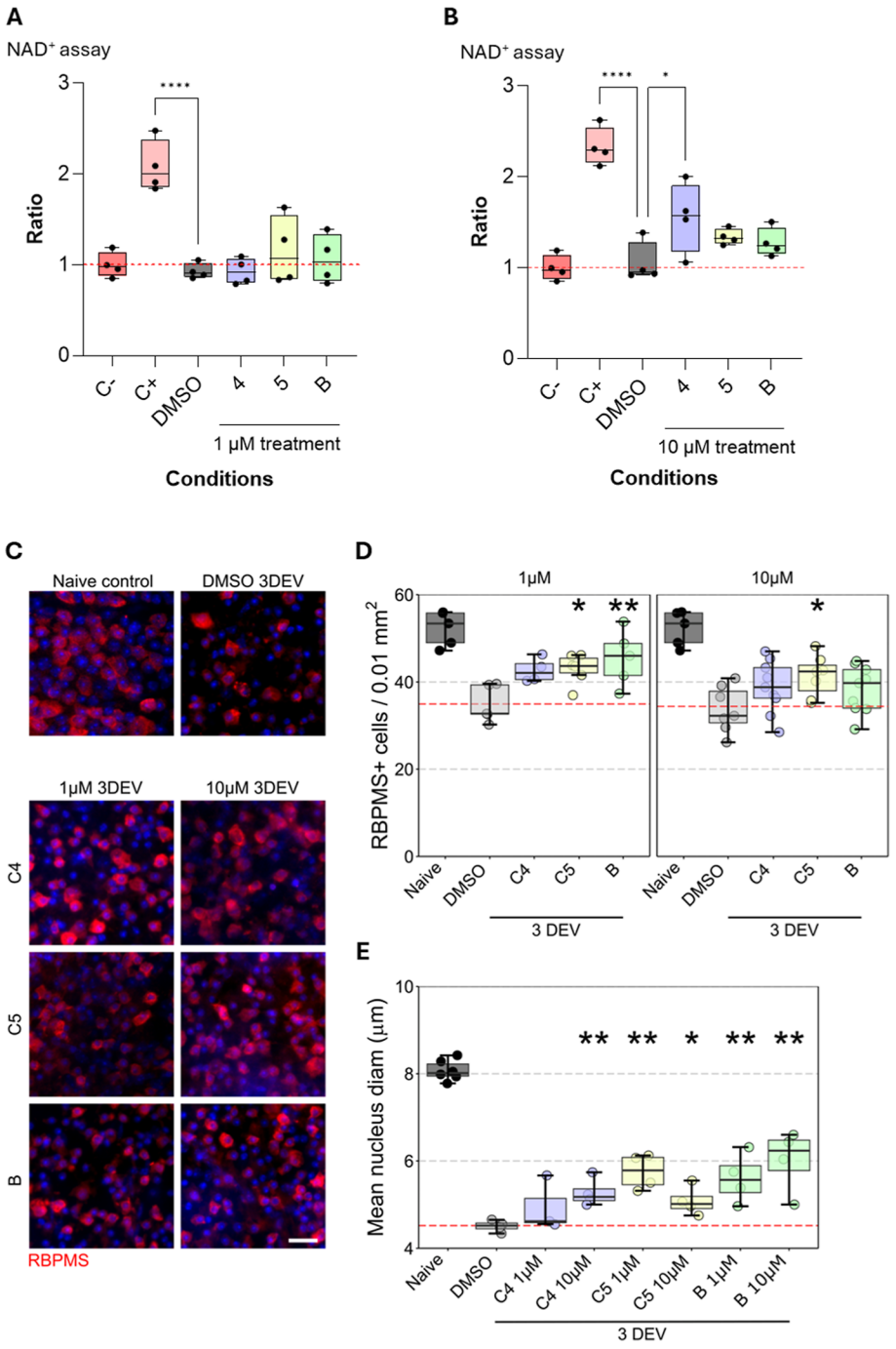


Figure 5. Compound **4**, **5**, and **B** are neuroprotective in an axotomy model. (A,B) Dissociated cortex was incubated with compounds **4**, **5**, or **B** at 1 (A) or 10 μM (B) for 2 hours. NAD was measured and compared to the DMSO-only (vehicle)-treated cortex. Data from three independent experiments are shown as means ± SD, $n = 3$. (C–E) To assess the neuroprotective potential of these compounds, we used the retinal explant model. At 3 DEV, compounds **5** and **B** demonstrated significant RGC neuroprotection at 1 μM compared to DMSO-only (vehicle)-treated retinas (D). This was maintained at 10 μM for compound **5**. To assess the health of these surviving cells, we measured the average nuclear diameter. At 3 DEV (days ex vivo), compounds **5** and **B** demonstrated significant protection against nuclear shrinkage at 1 μM compared to DMSO-only (vehicle)-treated retinas (C,E). Compound **4** demonstrated significant protection against nuclear shrinkage at 10 μM compared to DMSO-only (vehicle)-treated retinas. Data from three independent experiments are shown as means ± SD, $n = 3$. ****$P < 0.0001$, **$P < 0.001$, *$P < 0.05$.

In the next step, we assessed the neuroprotective potential of these compounds and used a retinal explant model (Figure 5C–E).[35,36] Here, enucleation of the eye severs the optic nerve, triggering a neurodegenerative cascade in all retinal ganglion cells (RGCs) in the retina. RGC death is primarily driven by Wallerian degeneration, a retrograde cascade of axon degeneration. This mechanism is highly dependent on the balance of axonal levels of NAD and its precursor nicotinamide mononucleotide (NMN) and can be triggered by mitochondrial dysfunction.[37] Interventions that increase NAD or limit NAD consumption are protective against Wallerian degeneration and provide neuroprotection in this model.[36] RGC

Downloaded from pubs.acs.org/jmcmar/article-pdf/69/20/23517/6749327/jm6c00526.pdf by UNIV OF SHEFFIELD user on 10 November 2026

https://doi.org/10.1021/acs.jmedchem.6c00526
J. Med. Chem. 2026, 69, 23517–23539

neurodegeneration reaches ~30−40% over 3 days ex vivo (DEV), providing a window to test neuroprotective candidates by their incubation in the culture media.[35,36] At 3 DEV, **5** and **B** demonstrated significant RGC neuroprotection at 1 μM compared to vehicle (DMSO)-treated retinas (Figure 5C−D). This was maintained at 10 μM for **5** (Figure 5C−E), and an increase in RGC neuroprotection was also maintained for **4** at 10 μM, however, not significantly. To assess the health of these surviving cells, we measured the average nuclear diameter of DAPI-stained nuclei as significant pre-aprotic nuclear shrinkage occurs in this experimental model.[35] At 3 DEV, **5** and **B** demonstrated significant protection against nuclear shrinkage at 1 μM compared to vehicle-only (DMSO)-treated retinas (Figure 5E). **4** demonstrated significant protection against nuclear shrinkage at 10 μM compared to vehicle (DMSO)-treated retinas (Figure 5E).

Our results demonstrate that all compounds offer some level of neuroprotection in the retinal explant model. Although, at 1 μM, there was no NAD boosting effect, the concentrations may not be directly comparable across experimental settings and may provide a benefit over a longer time period of 3 days. The compounds could also provide neuroprotection more indirectly by improving mitochondrial resilience against insult and thereby limiting mitochondrial dysfunction triggered Wallerian degeneration.

DISCUSSION AND CONCLUSIONS

In this study, we identify and characterize mitochondrial enriched OGG1 organocatalytic switches that protect mitochondrial function and confer neuroprotection in a retinal axotomy model that induces mitochondrial dysfunction. Building on previous work demonstrating that OGG1-ORCAs can rewire OGG1 into a highly efficient AP lyase and modulate transcriptional and repair processes primarily in the nuclear compartment,[14,16,20,22,23] we here extend this concept to the mitochondria.

Building on the first-generation ORCAs, the present optimization retained the 3,4-dichloroaniline recognition motif responsible for high-affinity engagement of the OGG1 active site while focusing optimization on the catalytic heterocycle.[16,20] This strategy allowed modulation of catalytic properties without disrupting the binding mode previously established by crystallography. Unlike previous optimization campaigns aimed primarily at maximizing catalytic activation, the present series was designed to improve mitochondrial activity while preserving chemical switching. Introduction of fused and partially saturated heterocycles was guided by the hypothesis that increasing heterocyclic basicity, conformational rigidity, and hydrogen-bonding capacity could improve mitochondrial exposure while maintaining productive active-site interactions. Pyrazoles, pyridines, and related bicyclic analogues were selected to probe how heterocycle basicity, orientation of ring nitrogens, and conformational restriction influence the proton abstraction required for β-elimination. Because ORCA catalysis relies on transient participation in the OGG1 reaction Schiff Base state and not simple occupancy of the active site, relatively subtle electronic differences were expected to influence catalytic efficiency more strongly than equilibrium binding affinity. Despite substantial modification of the catalytic heterocycle, activation potency remained remarkably robust across the series, indicating that productive organocatalysis tolerates considerable electronic and steric variation, provided that active-site recognition is maintained.

Whereas first-generation ORCAs established that OGG1 could be chemically reprogrammed into an efficient AP lyase, the present chemical series addresses a distinct medicinal chemistry objective: identifying compounds capable of exerting this effect within the mitochondrial compartment while maintaining favorable developability properties. The optimization therefore prioritized cellular phenotype, mitochondrial function, and physicochemical performance over further increases in biochemical potency, ultimately identifying compound **4** as a balanced lead for mitochondrial applications.

Using a phenotypic screen centered on the MMP in conditions of oxidative stress, we discovered pyrazole-based OGG1-ORCAs, exemplified by compound **4** and its methyl analogue **5**, that act from within the OGG1 active site, rescue mitochondrial function and morphology, increase NAD levels, and attenuate neurodegeneration. Together, these findings demonstrate that catalytic reprogramming of OGG1 is associated with improved mitochondrial resilience and neuronal survival under oxidative stress. While the molecular coupling between altered BER catalysis and mitochondrial homeostasis remains to be fully resolved, our data identify OGG1 catalytic enhancement as a pharmacologically tractable strategy for preserving mitochondrial function.[1]

Mechanistically, ORCAs appear to accelerate turnover of the OGG1 reaction cycle by enhancing AP lyase chemistry after lesion recognition. Rather than increasing lesion recognition itself, this shifts the rate-limiting step of base excision repair toward downstream processing by APE1. We therefore propose that ORCAs increase BER flux rather than altering lesion specificity. Although mitochondrial BER flux was not directly measured here, this model is consistent with the observed improvements in mitochondrial physiology.

The PAGE-based analysis with radioactively labeled DNA confirmed that the present series efficiently generates 3′-PUA products, indicating an efficient δ-elimination and validating that this scaffold can render OGG1 a robust AP lyase. The plateauing of OGG1 incision rate against 8-oxoG substrates and the loss of activation in selected active-site mutants further indicate that the compounds operate from within the catalytic center and do not stabilize a DNA−protein complex or act through indirect mechanisms. The X-ray co-crystal structure of **4** in complex with OGG1 corroborates this conclusion, revealing a binding mode that overlaps with previously described ORCAs[14] and is supported by multiple hydrogen bonds, π-stacking, and hydrophobic interactions within the active site. Importantly, the mutational sensitivity pattern, with loss of activation in Phe319Ala and Lys249Trp but maintained enhancement in Ser326Cys and Asp268Ala, suggests that the compound requires an intact active site pocket but tolerates certain catalytically relevant rearrangements, in line with its organocatalytic mechanism rather than simple allosteric modulation.[19,30,31]

Selectivity profiling and physicochemical characterization demonstrate that **4** fulfils key properties of a drug-like mitochondrial OGG1 modulator. In OGG1 knockout U2OS cells, **4** lost its ability to rescue MMP, indicating a high degree of dependence on OGG1 for its cellular effect. Compound **5** retained partial mitochondrial activity in OGG1-deficient cells, indicating that modest structural modification can reduce target specificity while preserving the cellular phenotype. Accordingly, compound **4** served as the principal mechanistic probe throughout the study, whereas compound **5** primarily informs the medicinal chemistry SAR. Nonetheless, both compounds

Downloaded from pubs.acs.org/jmcmar/article-pdf/69/20/23517/6749327/jm6c00526.pdf by UNIV OF SHEFFIELD user on 10 November 2026

https://doi.org/10.1021/acs.jmedchem.6c00526
J. Med. Chem. 2026, 69, 23517−23539

showed robust rescue in wild-type cells and in non-transformed RPE1 cells, with preserved cell confluency at functionally active concentrations. Importantly, the LC/MS measurement was not intended to define a fold-enrichment relative to the cytosol but to determine whether **4** reaches a pharmacologically relevant concentration within the mitochondrial fraction. The measured mitochondrial exposure exceeded the biochemical AC_{50} of **4** by approximately 35-fold, indicating that mitochondrial levels of **4** are sufficient to support robust OGG1 activation. Thus, the ~35-fold value represents the exposure margin relative to the biochemical activation concentration rather than a mitochondrial accumulation factor. Further, the absence of relevant inhibition across a panel of DNA glycosylases and NUDIX proteins, combined with narrow kinase engagement primarily for the negative control **7**, further support a focused target profile. From a developability standpoint, **4** displays favorable lipophilicity, solubility, clearance, and permeability, all compatible with mitochondrial entry and sustained intracellular activity. The added second nitrogen center appears to be an important design element, complementing active-site affinity and the catalytic center to enhance mitochondrial delivery while preserving OGG1 selectivity.

Functionally, mito-ORCAs preserved mitochondrial function under oxidative stress at multiple levels. In a PQ-driven model of mitochondrial dysfunction, **4** and **5** robustly rescued the MMP in U2OS and RPE1 cells to an extent comparable or superior to that of the previously reported activator **B**.[19,21] At the same time, compounds that lacked stimulating activity on OGG1 or active-site compatibility, such as **7** and **8**, were inactive in restoring MMP, strengthening the link between OGG1 AP lyase activation and mitochondrial rescue. Beyond membrane potential, **4** also normalized mitochondrial morphology and cellular ROS levels in conditions of PQ- and menadione-induced stress, respectively. Oxidative insults typically fragment the mitochondrial network, promoting smaller, damaged organelles and perpetuating ROS production.[33] In line with this, PQ increased the number of mitochondrial fragments per cell, while **4** reduced fragmentation toward control levels, as shown by confocal microscopy. The lack of an effect of TH10785 on mitochondrial morphology emphasizes that not all OGG1 modulators are equivalent in the mitochondria and that mitochondrial enrichment is required to achieve this phenotype. In addition, yet undiscovered off-targets may exist for OGG1 targeting compounds, as previously shown for scaffolds represented by reported OGG1 inhibitors.[38,39] Furthermore, **4** significantly reduced cellular ROS after menadione challenge, whereas TH10785 did not, linking mitochondrial OGG1 activity to a reduction of oxidative burden. Together, these findings indicate that catalytic enhancement of mitochondrial OGG1 is sufficient to preserve multiple independent indicators of mitochondrial health, including membrane potential, network morphology, and oxidative burden. Although the precise molecular sequence linking enhanced BER to these phenotypes remains to be elucidated, the concordance of these independent readouts strongly supports improved mitochondrial homeostasis as the dominant cellular consequence of ORCA treatment.

Our findings further support an emerging role of mitochondrial OGG1 as a determinant of mitochondrial homeostasis beyond its established function in DNA repair. Previous genetic studies have shown that mitochondrial overexpression of OGG1 improves oxidative phosphorylation, preserves metabolic fitness, and protects against oxidative stress.[10−12] Here, we demonstrate that pharmacological enhancement of endogenous OGG1 recapitulates several of these protective phenotypes, linking catalytic activation of OGG1 to mitochondrial resilience. Short-term treatment of dissociated cortical neurons with **4**, **5**, and **B** significantly increased NAD levels, with **4** eliciting the strongest effect at 10 μM. In the context of Wallerian degeneration, axonal survival depends on the balance between NAD synthesis (e.g. via NMNAT2) and NAD consumption, with mitochondrial dysfunction accelerating NAD depletion and triggering SARM1-dependent axon degeneration.[36,37] Consistent with this model, all three compounds conferred neuroprotection in a retinal explant axotomy model, reducing RGC loss and preserving nuclear morphology. Notably, **5** and **B** were effective at 1 μM, a concentration at which no significant NAD increase was detected in acute assays, suggesting that modest or more slowly developing changes in NAD metabolism, improved mitochondrial resilience, or reduced NAD consumption over several days may be sufficient to delay degeneration. **4** showed more pronounced protection at 10 μM, aligning with its robust NAD boosting capacity. While the exact contribution of NAD modulation versus improved mitochondrial quality control remains to be dissected, our data imply that targeting OGG1 at the mitochondria intersects with the metabolic pathways governing Wallerian degeneration.

The present work expands the therapeutic scope of OGG1 modulation beyond its established roles in nuclear DNA repair, inflammatory transcriptional regulation, and cancer biology.[7−9,14,17,40] Rather than inhibiting OGG1, mito-ORCAs exploit the catalytic enhancement of endogenous DNA repair to preserve mitochondrial function under oxidative stress. Although the precise molecular sequence linking enhanced BER catalysis to mitochondrial homeostasis remains to be fully elucidated, our data consistently demonstrate improvements across multiple independent measures of mitochondrial health, including membrane potential, network morphology, oxidative burden, NAD levels, and neuronal survival. Together with previous genetic studies demonstrating protective effects of mitochondrial OGG1 overexpression,[10−12] these findings support catalytic enhancement of OGG1 as a pharmacologically tractable strategy for improving mitochondrial resilience. Given the central role of mitochondrial dysfunction and oxidative DNA damage in ageing and neurodegeneration[1,33,41] and the importance of NAD homeostasis in neuronal survival and axonal maintenance,[36,37,42,43] mito-ORCAs represent a mechanistically distinct class of candidate therapeutics that warrant further investigation across diseases characterized by mitochondrial oxidative stress and impaired mtDNA maintenance.

EXPERIMENTAL SECTION

General Information Chemical Synthesis

All reagents and solvents were purchased from commercial vendors and used without further purification. Unless otherwise stated, reactions were performed without care to exclude air or moisture. Analytical thin-layer chromatography was performed on silica gel 60 Å F-254 plates (E. Merck) and visualized under a UV lamp. Flash column chromatography was performed in a Biotage SP1 MPLC system using Fisher Chemical silica gel 60 Å. ^{1}H and ^{13}C NMR spectra were recorded on Bruker DRX-400 MHz or Bruker Ascend 400 MHz spectrometers. Chemical shifts are expressed in parts per million (ppm) and referenced to the residual solvent peak (^{1}H: δ 7.26 for CDCl3, δ 2.50 for DMSO-d_6, δ 3.31 for methanol-d_4; ^{13}C: δ 29.84 for CDCl3, δ 39.52 for DMSO-d_6, and δ 49.00 for methanol-d_4). Analytical LC−MS were performed either on an Agilent MSD mass spectrometer connected to an Agilent 1100 system or an Agilent 1260 infinity II with a G6125B mass

Downloaded from pubs.acs.org/jmcmar/article-pdf/69/20/23517/6749327/jm6c00526.pdf by UNIV OF SHEFFIELD user on 10 November 2026

https://doi.org/10.1021/acs.jmedchem.6c00526
J. Med. Chem. 2026, 69, 23517−23539

spectrometer. Columns used were ACE 3C8 (50 × 3.0 mm), where H_2O (+0.1% TFA) and MeCN were used as mobile phases at a flow rate of 1 mL/min, or an Xterra MSC18 (50 × 3.0 mm) column where H_2O (10 mM NH_4HCO_3; pH = 10) and MeCN were used as mobile phases at a flow rate of 1 mL/min. For LC−MS, detection was made by UV and MS (ESI+). Preparative LC was performed on a Gilson system using a Waters C18 OBD 5 μm column (30 × 75 mm) with water buffer (50 mM NH_4HCO_3 at pH 10) and MeCN as mobile phases using a flow rate of 45 mL/min or an ACE 5C8 (100 × 21.2 mm) column with water buffer (0.1% TFA) and MeCN as mobile phases using a flow rate of 30 mL/min. All final compounds were assessed to be >95% pure by LC−MS analysis. Compounds in our nucleobase/nucleoside/nucleotide and prior art screening set were not resynthesized, and no characterization was performed. Compounds available through NCI DTP were not resynthesized, and no characterization was performed. High-resolution mass spectra (HRMS) were measured with EI or ESI ionization. A chromatographic purification was performed before each measurement. The Thermo Q-Exactive plus device for ESI-mass spectra was coupled to a binary UHPLC system. For EI-measurement, a GC-system was coupled to the Thermo Q-Exactive GC device.

General Procedure for the Preparation of Compounds and Their Characterization (1−17)

***N*-(3,4-Dichlorophenyl)thieno[3,2-*b*]pyridin-7-amine (1).** A mixture of 7-chlorothieno[3,2-*b*]pyridine (25.4 mg, 0.15 mmol, 1 equiv.) and 3,4- dichloroaniline (27.5 mg, 0.17 mmol, 1.1 equiv.), was dissolved in TFE (1.2 mL, 50 V). The reaction vessel was flushed with nitrogen before and after the addition of trifluoroacetic acid (17.6 μL, 0.23 mmol, 1.5 equiv.). The reaction mixture was stirred at 80 °C for 16 hours. After 16 h, the crude mixture was basified with excess aq. NaHCO3, resulting in a white precipitate. Distilled water (ca. 3 mL) was added to the suspension with vigorous stirring for 10 minutes. The remaining solid was filtered under vacuum and recrystallized from EtOAc to afford the final product. Yield: 35% as an off-white crystal. ^{1}H NMR (400 MHz, DMSO-d_6): δ 9.08 (s, 1H), 8.39 (d, J = 5.4 Hz, 1H), 8.03 (d, J = 5.5 Hz, 1H), 7.59 (d, J = 8.7 Hz, 1H), 7.48 (d, J = 5.6 Hz, 1H), 7.47 (d, J = 2.8 Hz, 1H), 7.27 (dd, J = 8.7, 2.6 Hz, 1H), 7.01 (d, J = 5.4 Hz, 1H). ^{13}C{^{1}H} NMR (151 MHz, DMSO-d_6): δ 157.82, 148.37, 144.80, 140.84, 131.41, 130.95, 130.49, 125.20, 124.13, 122.04, 121.00, 120.74, 103.63. HRMS (ESI): m/z calcd for $C_{13}H_9Cl_2N_2S$ [M + H]$^+$: 294.9858; found, 294.9855.

***N*-(3,4-Dichlorophenyl)quinolin-4-amine (2).** A mixture of 4-chloroquinoline (24.5 mg, 0.15 mmol, 1 equiv.) and 3,4-dichloroaniline (27.5 mg, 0.17 mmol, 1.1 equiv.), was dissolved in TFE (1.2 mL, 50 V). The reaction vessel was flushed with nitrogen before and after the addition of trifluoroacetic acid (17.6 μL, 0.23 mmol, 1.5 equiv.). The reaction mixture was stirred at 80 °C for 16 hours. After 16 h, the crude mixture was basified with excess aq. $NaHCO_3$, resulting in a white precipitate. Distilled water (ca. 3 mL) was added to the suspension with vigorous stirring for 10 minutes. The remaining solid was filtered under vacuum and recrystallized from EtOAc to afford the final product. Yield: 46% as a pale-yellow crystal. ^{1}H NMR (400 MHz, DMSO-d_6): δ 9.13 (s, 1H), 8.56 (d, J = 5.2 Hz, 1H), 8.31 (d, J = 8.4 Hz, 1H), 7.92 (d, J = 8.3 Hz, 1H), 7.77−7.70 (m, 1H), 7.61 (d, J = 8.7 Hz, 1H), 7.57 (d, J = 2.4 Hz, 1H), 7.60−7.53 (m, 1H), 7.37 (dd, J = 8.7, 2.6 Hz, 1H), 7.10 (d, J = 5.2 Hz, 1H). ^{13}C{^{1}H} NMR (151 MHz, DMSO-d_6): δ 150.76, 148.98, 146.29, 141.46, 131.56, 131.06, 129.45, 129.30, 125.07, 124.15, 122.34, 122.09, 120.96, 120.17, 103.24. HRMS (ESI): m/z calcd for $C_{15}H_{10}Cl_2N_2$ [M + H]$^+$: 289.0294; found, 289.0294.

***N*-(3,4-Dichlorophenyl)thieno[2,3-*b*]pyridin-4-amine (3).** A mixture of 4-chlorothieno[2,3-*b*]pyridine (25.4 mg, 0.15 Mmol, 1 equiv.) and 3,4-dichloroaniline (27.5 mg, 0.17 Mmol, 1.1 equiv.) was dissolved in 2,2,2-trifluoroethanol (1.2 mL, 50 V). The reaction vessel was flushed with nitrogen before and after the addition of trifluoroacetic acid (17.6 μL, 0.23 Mmol, 1.5 equiv.) in (1.2 mL). The reaction mixture was stirred at 80 °C for 24 hours. The reaction was quenched with *N*,*N*′-diisopropylethylamine (DIPEA, 1.5 equiv.) and then cooled to room temperature and concentrated under reduced pressure. The crude residue was purified by flash/column chromatography to afford the desired product. Yield: 19% as an off-white powder. ^{1}H NMR (400 MHz, Acetone-*d6*): δ 8.45−8.22 (M, 2H), 7.65−7.50 (M, 4H), 7.36 (dd, J = 8.7, 2.5 Hz, 1H), 7.11 (dd, J = 5.4, 2.8 Hz, 1H). ^{13}C{^{1}H} NMR (151 MHz, DMSO-d_6): δ 162.55, 147.67, 144.80, 140.84, 131.56, 131.12, 124.31, 124.15, 122.16, 121.76, 120.80, 119.30, 102.70. HRMS (ESI): m/z calcd for $C_{13}H_7Cl_2N_2S$ [M − H]$^-$: 292.9712; found, 292.9702.

***N*-(3,4-Dichlorophenyl)-1*H*-pyrazolo[3,4-*b*]pyridin-4-amine (4).** A mixture of 4-chloro-1*H*-pyrazolo[3,4-*b*]pyridine (1.5 g, 0.00976 mol, 1.0 equiv.) and 3,4-dichloroaniline (2.72 g, 0.01074 mol, 1.1 equiv.) was dissolved in ethanol (75 mL, 50 V). The reaction vessel was flushed with nitrogen before and after the addition of trifluoroacetic acid (1.12 mL, 0.01464 mol, 1.5 equiv.). The reaction mixture was stirred at 85 °C for 16 hours. The reaction was quenched with *N*,*N*′-diisopropylethylamine (DIPEA, 1.5 equiv.) and then cooled to room temperature, filtered, and washed with ethanol. The obtained solid was then dried to get the desired product. Yield: 80% as a white solid. ^{1}H NMR (DMSO-d_6, 400 MHz): δ 13.35 (1H, s), 9.42 (1H, s), 8.17 (1H, d, J = 5.4 Hz), 8.13 (1H, s), 7.63 (1H, d, J = 8.7 Hz), 7.54 (1H, d, J = 2.6 Hz), 7.35 (1H, dd, J = 8.7, 2.6 Hz), 6.72 (1H, d, J = 5.4 Hz). ^{13}C{^{1}H} NMR (151 MHz, DMSO-d_6): δ 153.44, 147.53, 143.41, 137.78, 132.60, 132.23, 129.71, 129.49, 126.72, 125.17, 106.42, 97.21, HRMS (ESI): m/z calcd for $C_{12}H_8Cl_2N_4$ [M + H]$^+$: 279.0199; found, 279.0198.

***N*-(3,4-Dichlorophenyl)-1-Methyl-1*H*-pyrazolo[3,4-b] pyridin-4-amine (5).** A mixture of *N*-(3,4-dichlorophenyl)-1*H*-pyrazolo[3,4-*b*]pyridin-4-amine (100 mg, 0.3597 Mmol, 1.0 equiv.) and cesium carbonate (234 mg, 0.7194 Mmol, 2 equiv.) was dissolved in DMF (1.5 mL, 15 V) and stirred for 30 min at room temperature. After 30 min, methyl iodide (29 μL, 0.4676, 1.3 equiv.) was added, and the resulting reaction mixture was again stirred at room temperature for 24 hours. The reaction mixture was then partitioned between water and ethyl acetate and extracted 3 times; the obtained organic solution was then concentrated under reduced pressure. The crude product was purified by flash/column chromatography to afford the final compound. Yield: 60% as an off white solid. ^{1}H NMR (400 MHz, DMSO-d_6): δ 9.46 (S, 1H), 8.19 (d, J = 5.3 Hz, 1H), 8.11 (S, 1H), 7.61 (d, J = 8.7 Hz, 1H), 7.53 (d, J = 2.5 Hz, 1H), 7.33 (dd, J = 8.7, 2.6 Hz, 1H), 6.73 (d, J = 5.5 Hz, 1H), 3.97 (S, 2H). ^{13}C{^{1}H} NMR (151 MHz, DMSO-d_6): δ 151.76, 149.84, 144.04, 140.45, 131.58, 131.12, 130.07, 124.71, 122.31, 121.01, 105.73, 98.67, 33.59. HRMS (ESI): m/z calcd for $C_{13}H_{10}Cl_2N_4$ [M + H]$^+$: 293.0355; found, 293.0352.

***N*-(3,4-Dichlorophenyl)-6,7-dihydro-5*H*-cyclopenta[*b*] pyridin-4-amine (6).** A suspension of 4-chloro-6,7-dihydro-5*H*-cyclopenta[*b*]pyridine (49.5 μL, 0.40 Mmol, 1.0 equiv.), 3,4-dichloroaniline (74.5 mg, 0.46 Mmol, 1.15 equiv.), and sodium tert-butoxide (47.1 mg, 0.49 Mmol, 1.23 equiv.) in toluene (1.4 mL) was sparged with N_2 for 10 minutesin. $Pd(dba)_2$ (9.6 mg, 4 mol %) and JohnPhos (8.4 mg, 7 mol %) were added before further sparging of the mixture for 10 minutes. The reaction vial was sealed and heated at 85 °C for 3 days. The black mixture was cooled to rt, filtered through celite, and washed with EtOAc (ca. 2 mL). The filtrate was concentrated in vacuo and purified using prep HPLC (60 − 80% MeCN/H_2O w/ NH_4HCO_3 50 mM Buffer). Appropriate fractions were collected and evaporated to yield the desired product. Yield: 33% as a white powder. ^{1}H NMR (400 MHz, DMSO-d_6): δ 8.31 (S, 1H), 8.03 (d, J = 5.6 Hz, 1H), 7.53 (d, J = 8.7 Hz, 1H), 7.35 (d, J = 2.6 Hz, 1H), 7.17 (dd, J = 8.8, 2.6 Hz, 1H), 6.84 (d, J = 5.7 Hz, 1H), 2.85 (T, J = 7.7 Hz, 2H), 2.78 (T, J = 7.3 Hz, 2H), 2.03 (P, J = 7.6 Hz, 2H). ^{13}C{^{1}H} NMR (151 MHz, DMSO-d_6): δ 165.92, 148.32, 145.43, 141.54, 131.35, 130.86, 123.11, 123.04, 120.91, 119.58, 106.51. HRMS (ESI): m/z calcd for $C_{14}H_{12}Cl_2N_2$ [M + H]$^+$: 279.0450; found, 279.0449.

***N*-(3,4-Dichlorophenyl)-1*H*-pyrazolo[4,3-c]pyridin-4-amine (7).** A mixture of 4-chloro-1*H*-pyrazolo[4,3-*c*]pyridine (100 mg, 0.6511 Mmol, 1.0 equiv.) and 3,4-dichloroaniline (116 mg, 0.7162, 1.1 equiv.) was flushed with nitrogen and stirred at 100 °C for 24 hours and then cooled to room temperature. The reaction was diluted by adding

Downloaded from pubs.acs.org/jmcmar/article-pdf/69/20/23517/6749327/jm6c00526.pdf by UNIV OF SHEFFIELD user on 10 November 2026

https://doi.org/10.1021/acs.jmedchem.6c00526
J. Med. Chem. 2026, 69, 23517−23539

methanol, quenched with *N,N′*-diisopropylethylamine (DIPEA, 1.5 equiv.), and concentrated under reduced pressure. The crude residue was purified by flash/column chromatography to afford the desired product. Yield: 55.8% as a light-yellow Solid. ^{1}H NMR (400 MHz, DMSO-d_6): δ 13.34 (S, 1H), 9.55 (S, 1H), 8.46 (d, J = 2.6 Hz, 1H), 8.44 (d, J = 1.0 Hz, 1H), 7.93 (d, J = 6.0 Hz, 1H), 7.86 (dd, J = 8.9, 2.6 Hz, 1H), 7.55 (d, J = 8.9 Hz, 1H), 6.99 (dd, J = 6.0, 1.0 Hz, 1H). ^{13}C{^{1}H} NMR (151 MHz, DMSO-d_6): δ 148.96, 144.06, 141.92, 141.39, 132.45, 130.66, 130.24, 122.02, 119.75, 118.86, 108.97, 98.68. HRMS (ESI): m/z calcd for $C_{12}H_8Cl_2N_4$ [M + H]$^+$: 279.0199; found, 279.0193.

***N*-(3,4-Dichlorophenyl)-1*H*-indol-4-amine (8).** A suspension of 1*H*-indol-4-amine (100 mg, 0.7566 Mmol, 1.0 equiv), 4-bromo-1,2-dichlorobenzene (188 mg, 0.8323 Mmol, 1.1 equiv), $Pd(dba)_3$ (21 mg, 0.0226 Mmol, 3 mol %), $Pd(OAc)_2$ (5 mg, 0.0226 Mmol, 3 mol %), xantphos (53 mg, 0.0907 Mmol, 12 mol %), and cesium carbonate (520 mg, 1.588 Mmol, 2.1 equiv) in toluene (1.5 mL, 15 V) was sparged with nitrogen for 10 minutes. The reaction vial was sealed and heated at 100 °C for 3 hours. After cooling to room temperature, the reaction mixture was filtered through celite and rinsed with DCM. The combined filtrate was then partitioned between water and DCM and extracted 3 times; the obtained organic solution was then concentrated under reduced pressure. The crude product was purified by flash/column chromatography to afford the final compound. Yield: 36.2% as a brown powder. ^{1}H NMR (400 MHz, DMSO-d_6): δ 11.13 (S, 1H), 8.37 (S, 1H), 7.37 (d, J = 8.8 Hz, 1H), 7.27 (T, J = 2.8 Hz, 1H), 7.14 (d, J = 2.6 Hz, 1H), 7.11 (d, J = 8.1 Hz, 1H), 7.06−6.95 (M, 2H), 6.83 (d, J = 7.4 Hz, 1H), 6.40 (T, J = 2.6 Hz, 1H). ^{13}C{^{1}H} NMR (151 MHz, DMSO-d_6): δ 145.31, 137.26, 133.48, 131.10, 130.56, 124.06, 121.54, 121.00, 118.79, 116.28, 115.57, 108.40, 106.45, 99.39. HRMS (ESI): m/z calcd for $C_{14}H_{10}Cl_2N_2$ [M + H]$^+$: 277.0294; found, 277.0290.

5-(3,4-Dichlorophenyl)-1*H*-pyrrolo[2,3-*b*]pyridine (9). A suspension of 5-bromo-1*H*-pyrrolo[2,3-*b*]pyridine (100 mg, 0.5075 mmol, 1.0 equiv), (3,4-dichlorophenyl)boronic acid (116 mg, 0.6090 mmol, 1.2 equiv), $Pd(dppf)Cl_2$ (18.6 mg, 0.0253 mmol, 5 mol %), and potassium carbonate (210 mg, 1.522 mmol, 3 equiv) in dioxane/water (5 mL {2.5:1}) was sparged with nitrogen for 10 minutes. The reaction vial was sealed and heated at 80 °C for 22 h. After cooling to room temperature, the reaction mixture was filtered through celite and rinsed with DCM. The combined filtrate was then partitioned between water and DCM and extracted 3 times; the obtained organic solution was then concentrated under reduced pressure. The crude product was purified by flash/column chromatography to afford the final compound. Yield: 74.1% as a white powder. ^{1}H NMR (400 MHz, DMSO-d_6): δ 11.79 (s, 1H), 8.55 (d, J = 2.3 Hz, 1H), 8.27 (d, J = 2.2 Hz, 1H), 7.99 (d, J = 1.9 Hz, 1H), 7.71−7.70 (m, 2H), 7.54 (dd, J = 3.5, 2.5 Hz, 1H), 6.51 (dd, J = 3.4, 1.9 Hz, 1H). ^{13}C{^{1}H} NMR (151 MHz, DMSO-d_6): δ 148.36, 141.42, 139.86, 131.69, 130.94, 129.51, 128.50, 127.30, 126.97, 126.40, 125.58, 119.63, 100.34. HRMS (ESI): m/z calcd for $C_{13}H_8Cl_2N_2$ [M + H]$^+$: 263.0137; found, 264.0084.

***N*-(3-Chloro-4-fluorophenyl)-1*H*-pyrazolo[3,4-*b*]pyridin-4-amine (10).** A mixture of 4-chloro-1*H*-pyrazolo[3,4-*b*]pyridine (23.0 mg, 0.15 Mmol, 1 equiv.) and 3-chloro-4-fluoroaniline (24.7 mg, 0.17 Mmol, 1.1 equiv.) was dissolved in 2,2,2-trifluoroethanol (1.2 mL, 50 V). The reaction vessel was flushed with nitrogen before and after the addition of trifluoroacetic acid (11.5 μL, 0.15 Mmol, 1.0 equiv.). The reaction mixture was stirred at 80 °C for 16 hours. The reaction was quenched with *N,N′*-diisopropylethylamine (DIPEA, 1.5 equiv.) and then cooled to room temperature and concentrated under reduced pressure. The crude residue was purified by flash/column chromatography to afford the desired product. Yield: 61% as a white powder. ^{1}H NMR (400 MHz, DMSO-d_6): δ 13.30 (S, 1H), 9.29 (S, 1H), 8.13−8.09 (M, 2H), 7.51−7.43 (M, 2H), 7.34 (ddd, J = 8.9, 4.2, 2.7 Hz, 1H), 6.58 (d, J = 5.4 Hz, 1H). ^{13}C{^{1}H} NMR (151 MHz, DMSO-d_6): δ 153.60 (d, J = 243.1 Hz), 153.64, 149.90, 144.73, 137.43 (d, J = 2.9 Hz), 131.43, 123.53, 122.36 (d, J = 7.0 Hz), 119.87 (d, J = 18.8 Hz), 117.49 (d, J = 22.0 Hz), 105.02, 97.80. HRMS (ESI): m/z calcd for $C_{12}H_8ClFN_4$ [M + H]$^+$: 263.0494; found, 264.0494.

***N*-(4-Chloro-3-fluorophenyl)-1*H*-pyrazolo[3,4-*b*]pyridin-4-amine (11).** A mixture of 4-chloro-1*H*-pyrazolo[3,4-*b*]pyridine (23.0 mg, 0.15 Mmol, 1 equiv.) and 4-chloro-3-fluoroaniline (24.7 mg, 0.17 Mmol, 1.1 equiv.) was dissolved in 2,2,2-trifluoroethanol (1.2 mL, 50 V). The reaction vessel was flushed with nitrogen before and after the addition of trifluoroacetic acid (11.5 μL, 0.15 Mmol, 1.0 equiv.). The reaction mixture was stirred at 80 °C for 16 hours. The reaction was quenched with *N,N′*-diisopropylethylamine (DIPEA, 1.5 equiv.) and then cooled to room temperature and concentrated under reduced pressure. The crude residue was purified by flash/column chromatography to afford the desired product. Yield: 49% as a white powder. ^{1}H NMR (400 MHz, DMSO-d_6): δ 13.35 (1H, s), 9.44 (1H, s), 8.16 (1H, d, J = 5.4 Hz), 8.15 (1H, d, J = 1.4 Hz), 7.57 (1H, t, J = 8.7 Hz), 7.35 (1H, dd, J = 11.3, 2.5 Hz), 7.24−7.16 (1H, m), 6.75 (1H, d, J = 5.4 Hz). ^{13}C{^{1}H} NMR (151 MHz, DMSO-d_6): δ 157.48 (d, J = 245.6 Hz), 153.64, 149.92, 143.77, 141.11 (d, J = 9.6 Hz), 131.48, 131.01, 117.85 (d, J = 2.9 Hz), 112.72 (d, J = 17.2 Hz), 108.93 (d, J = 23.6 Hz), 105.40, 98.70. HRMS (ESI): m/z calcd for $C_{12}H_8ClFN_4$ [M + H]$^+$: 263.0494; found, 263.0486.

***N*-(4-Chlorophenyl)-1*H*-pyrazolo[3,4-*b*]pyridin-4-amine (12).** A mixture of 4-chloro-1*H*-pyrazolo[3,4-*b*]pyridine (23.0 mg, 0.15 Mmol, 1 equiv.) and 4-chloroaniline (21.7 mg, 0.17 Mmol, 1.1 equiv.) was dissolved in 2,2,2-trifluoroethanol (1.2 mL, 50 V). The reaction vessel was flushed with nitrogen before and after the addition of trifluoroacetic acid (11.5 μL, 0.15 Mmol, 1 equiv.). The reaction mixture was stirred at 80 °C for 16 hours. The reaction was quenched with *N,N′*-diisopropylethylamine (DIPEA, 1.5 equiv.) and then cooled to room temperature and concentrated under reduced pressure. The crude residue was purified by flash/column chromatography to afford the desired product. Yield: 74% as a Yellow Powder. ^{1}H NMR (400 MHz, DMSO-d_6): δ 13.31 (1H, s), 9.35 (1H, s), 8.13 (2H, s), 7.46 (2H, d, J = 8.2 Hz), 7.36 (2H, d, J = 8.3 Hz), 6.62 (1H, d, J = 5.4 Hz). ^{13}C{^{1}H} NMR (151 MHz, DMSO-d_6): δ 149.45, 138.97, 131.45, 129.28, 127.29, 123.29, 105.16, 97.82. HRMS (ESI): m/z calcd for $C_{12}H_9ClN_4$ [M + H]$^+$: 245.0589; found, 245.0587.

***N*-(3-Chloro-4-iodophenyl)-1*H*-pyrazolo[3,4-b]pyridin-4-amine (13).** A mixture of 4-chloro-1*H*-pyrazolo[3,4-*b*]pyridine (100 mg, 0.6511 Mmol, 1 equiv.) and 3-chloro-4-iodoaniline (181 mg, 0.7162, 1.1 equiv.) was dissolved in 2,2,2-trifluoroethanol (5 mL, 50 V). The reaction vessel was flushed with nitrogen before and after the addition of trifluoroacetic acid (74 μL, 0.9766 Mmol, 1.5 equiv.). The reaction mixture was stirred at 85 °C for 16 hours. Showing complex side product formation, the reaction was quenched with *N,N′*-diisopropylethylamine (DIPEA, 1.5 equiv.) and then cooled to room temperature and concentrated under reduced pressure. The crude residue was purified by flash/column chromatography to afford the desired product. Yield: 28.2% as a light-yellow Powder. ^{1}H NMR (400 MHz, DMSO-d_6): δ 13.35 (S, 1H), 9.40 (S, 1H), 8.24−8.08 (M, 3H), 7.90 (d, J = 8.6 Hz, 1H), 7.51 (d, J = 2.5 Hz, 1H), 7.11 (dd, J = 8.6, 2.5 Hz, 1H), 6.73 (d, J = 5.4 Hz, 1H). ^{13}C{^{1}H} NMR (151 MHz, DMSO-d_6): δ 153.63, 149.93, 143.60, 141.97, 140.52, 137.82, 131.46, 121.08, 120.93, 105.42, 98.71, 89.87. HRMS (ESI): m/z calcd for $C_{12}H_8ClIN_4$ [M + H]$^+$: 370.9555; found, 370.9546.

***N*-Phenyl-1*H*-pyrazolo[3,4-*b*]pyridin-4-amine (14).** A mixture of 4-chloro-1*H*-pyrazolo[3,4-*b*]pyridine (76.8 mg, 0.50 mmol, 1 equiv.) and aniline (45.7 μL, 0.50 mmol, 1 equiv.) was dissolved in 2,2,2-trifluoroethanol (3.8 mL, 50 V). The reaction vessel was flushed with nitrogen before and after the addition of trifluoroacetic acid (42.1 μL, 0.55 Mmol, 1.1 equiv.). The reaction mixture was stirred at 80 °C for 16 hours. The reaction was quenched with *N,N′*-diisopropylethylamine (DIPEA, 1.5 equiv.) and then cooled to room temperature and concentrated under reduced pressure. The complex crude residue was purified by flash/column chromatography to afford a mix of unidentified compounds with the desired product among them. Yield: 22% as a Yellow Powder. ^{1}H NMR (400 MHz, DMSO-d_6): δ 13.23 (1H, s), 9.22 (1H, s), 8.11 (1H, s), 8.08 (1H, d, J = 5.5 Hz), 7.47−7.38 (2H, m), 7.34 (2H, dd, J = 8.5, 1.1 Hz), 7.22−7.07 (1H, m), 6.61 (1H, d, J = 5.5 Hz). ^{13}C{^{1}H} NMR (151 MHz, DMSO-d_6): δ 153.71, 149.77, 145.17, 140.01, 131.61, 129.36, 129.35, 129.33, 123.75,

Downloaded from pubs.acs.org/jmcmar/article-pdf/69/20/23517/6749327/jm6c00526.pdf by UNIV OF SHEFFIELD user on 10 November 2026

https://doi.org/10.1021/acs.jmedchem.6c00526
J. Med. Chem. 2026, 69, 23517−23539

121.95, 105.01, 97.60. HRMS (ESI): m/z calcd for $C_{12}H_{10}N_4$ $[M + H]^+$: 211.0978; found, 211.0977.

***N*-(3-Chloro-4-methoxyphenyl)-1*H*-pyrazolo[3,4-b]pyridin-4-amine (15).** A mixture of the 4-chloro-1*H*-pyrazolo[3,4-*b*]pyridine (23.0 mg, 0.15 mmol, 1 equiv.) and 3-chloro-4-methoxyaniline (26.8 mg, 0.17 mmol, 1.1 equiv.) was dissolved in 2,2,2-trifluoroethanol (1.2 mL, 50 V). The reaction vessel was flushed with nitrogen before and after the addition of trifluoroacetic acid (17.6 μL, 0.23 mmol, 1.5 equiv.). The reaction mixture was stirred at 80 °C for 16 hours. The reaction was quenched with *N*,*N*′-diisopropylethylamine (DIPEA, 1.5 equiv.) and then cooled to room temperature and concentrated under reduced pressure. The crude residue was purified by flash/column chromatography to afford the desired product. Yield: 38% as a gray powder. ^{1}H ^{1}H NMR (400 MHz, DMSO-d_6): δ 13.35 (S, 1H), 9.39 (S, 1H), 8.11 (S, 1H), 7.43−7.23 (M, 4H), 6.44 (d, J = 5.9 Hz, 1H), 3.89 (S, 3H). ^{13}C{^{1}H} NMR (151 MHz, DMSO-d_6): δ 154.04, 147.54, 143.25, 130.55, 129.35, 126.92, 125.53, 122.18, 114.18, 106.24, 96.37, 57.05. HRMS (ESI): m/z calcd for $C_{13}H_{11}ClN_4O$ $[M + H]^+$: 275.0694; found, 275.0692.

***N*-(3,4-Dichlorophenyl)-1*H*-pyrrolo[2,3-b]pyridin-4-amine (16).** A mixture of 4-chloro-1*H*-pyrrolo[2,3-*b*]pyridine (23 mg, 0.1513 mmol, 1.0 equiv.) and 3,4-dichloroaniline (27.5 mg, 0.1664, 1.1 equiv.) was dissolved in 2,2,2-trifluoroethanol (1.2 mL, 50 V). The reaction vessel was flushed with nitrogen before and after the addition of trifluoroacetic acid (34.7 μL, 0.4539 mmol, 3 equiv.). The reaction mixture was stirred at 85 °C for 72 H. The reaction was quenched with *N*,*N*′-diisopropylethylamine (DIPEA, 3 equiv.) and then cooled to room temperature and concentrated under reduced pressure. The crude residue was purified by flash/column chromatography to afford the desired product. Yield: 42.9% as an off-white powder. ^{1}H NMR (400 MHz, DMSO-d_6): δ 11.47 (S, 1H), 8.88 (S, 1H), 7.98 (d, J = 5.4 Hz, 1H), 7.54 (d, J = 8.8 Hz, 1H), 7.44 (d, J = 2.6 Hz, 1H), 7.27 (M, 2H), 6.76 (d, J = 5.4 Hz, 1H), 6.54 (d, J = 3.5 Hz, 1H). ^{13}C{^{1}H} NMR (151 MHz, DMSO-d_6): δ 149.89, 143.86, 142.01, 141.90, 131.33, 130.88, 122.95, 122.55, 120.41, 119.22, 109.52, 100.02, 98.12. HRMS (ESI): m/z calcd for $C_{13}H_9Cl_2N_3$ $[M + H]^+$: 278.0246; found, 278.0247.

***N*-(3,4-Dichlorophenyl)pyrazolo[1,5-a]pyrimidin-7-amine (17).** A mixture of 7-chloropyrazolo[1,5-*a*]pyrimidine (23.0 mg, 0.15 mmol, 1 equiv.) and 3,4-dichloroaniline (27.5 mg, 0.17 mmol, 1.1 equiv.) was dissolved in 2,2,2-trifluoroethanol (1.2 mL, 50 V). The reaction vessel was flushed with nitrogen before and after the addition of trifluoroacetic acid (17.6 μL, 0.23 Mmol, 1.5 equiv.). The reaction mixture was stirred at 80 °C for 24 hours. The reaction was quenched with *N*,*N*′-diisopropylethylamine (DIPEA, 1.5 equiv.) and then cooled to room temperature and concentrated under reduced pressure. The crude residue was purified by flash/column chromatography to afford the desired product. Yield: 37% as a white crystal. ^{1}H NMR (400 MHz, DMSO-d_6): δ 10.19 (S, 1H), 8.23−8.21 (M, 2H), 7.76 (d, J = 2.5 Hz, 1H), 7.70 (d, J = 8.7 Hz, 1H), 7.50 (dd, J = 8.7, 2.5 Hz, 1H), 6.58 (d, J = 2.3 Hz, 1H), 6.45 (d, J = 5.2 Hz, 1H). ^{13}C{^{1}H} NMR (151 MHz, DMSO-d_6): δ 149.94, 144.53, 143.63, 137.98, 131.59, 131.13, 127.06, 125.22, 123.66, 95.33, 87.32. HRMS (ESI): m/z calcd for $C_{12}H8Cl_2N_4$ $[M + H]^+$: 279.0199; found, 279.0198.

Chemical Compounds

The following commercial compounds were used: methyl viologen dichloride hydrate (Sigma), menadione (Sigma), and carbonyl cyanide 4-(trifluoromethoxy)phenylhydrazone (Sigma).

Biochemical Assay (Fluorescence). Enzymes were purified as below, and the biochemical assay including materials used was based on the publication by Visnes et al.[9] and "EUbOPEN" protocols (https://www.eubopen.org/protocols-reagents) and adapted where mentioned. OGG1 (10 nM) activation on the 10 nM substrate was monitored in a kinetic mode, and a time-resolved curve was obtained for each compound concentration in triplicates except where stated otherwise. Initial slopes were taken of the linear part of these curves to determine rates and kinetics. Fluorescence values of each compound concentration were normalized by the DMSO control values and calculated as % activation of the full turnover fluorescence of the APE (2 nM) control. The median activation concentration (AC_{50}) for each compound was calculated from the % activation of all tested concentrations and refers to the compound concentration that activates the reaction to 50% of the substrate turnover reached in the assay control coupled to APE1 (2 nM) as described before.[14]

Cell Culture. Cell lines were cultured at 37 °C in 5% CO_2. U2OS cells (2014; ATCC), BJ hTert and BJ hTert RASV12 (kindly gifted by W. Hahn, Dana Farber Cancer Institute), were cultured in DMEM (Life Technologies), and RPE1 cells were cultured in DMEM F-12 medium. Unless specified otherwise, all media were supplemented with 10% heat-inactivated FBS, 100 U ml^{-1} penicillin, and 100 μg m^{-1} streptomycin (Life Technologies). Cell lines were authenticated by the provider and cultivated according to the conditions specified, typically maintained in culture for 1 to 2 months before thawing of a new batch. Mycoplasma screening was performed routinely using the MycoAlert Mycoplasma Detection Kit (Lonza).

Resazurin Cell Viability. Compounds were dissolved in dimethylsulfoxide (DMSO) at 10 mM and dispensed to final concentrations in 384-well plates (corning) using a D300e digital dispenser (Tecan). Cells were seeded at 1000 (suspension and adherent cell lines) cells per well in 50 μl of complete medium. Plates were incubated in a humidified chamber for 96 h at 37 °C and 5% CO_2. Cell viability was determined by adding 10 μg ml^{-1} resazurin (Sigma-Aldrich) and measuring conversion to resorufin after 6 h. Fluorescence at 595 nm was measured with a Hidex Sense reader and Hidex Sense Software v.1.0 (Hidex Oy). Half-maximal effective concentration (EC_{50}) was calculated with logistic nonlinear regression in Prism v.9.3.1 (GraphPad).

Mitochondrial Membrane Potential. U2OS or RPE1cells were seeded at 5000 per well in 96-well plates in complete medium 2−3 days before imaging. The next day, cells were treated with compounds for 24 h. Before imaging, cells were washed with PBS and incubated with 20 nM tetramethylrhodamine methyl ester (TMRM) (Molecular Probes) and 10 μM verapamil (Sigma-Aldrich) for 30 min at 37 °C in complete media. Carbonyl cyanide *p*-trifluoromethoxyphenylhydrazone (FCCP, 20 μM, Sigma-Aldrich) was used as a positive control. Cells were imaged live with a Spark Cyto (Tecan) reader. TMRM fluorescence analysis in mitochondrial regions of interest was performed using CellProfiler.

Cellular ROS Measurements. U2OS cells were seeded in 35 mm dishes. The next day, cells were treated with 100 μM menadione for 1 h, followed by 2× PBS washes and incubation with 10 μM concentrations of compounds for 1 h. Before imaging, cells were washed with PBS and incubated with 20 nM CellROX (Molecular Probes) for 30 min at 37 °C in complete media. Cells were imaged live with a Zeiss LSM 780 confocal microscope using a 40× immersion oil objective. Image analysis was performed with ImageJ (NIH) and CellProfiler (Broad Institute, Cambridge, MA, USA) software.

MtDNA DX Measurement. U2OS cells were seeded in 96-well plates. The next day, cells were treated with compounds for 24 h. Following this, mtDNA lesion frequency was quantified using the developed PCR-based assay, Mito DNADX, as previously described in Qi et al., 2023.[32]

Mitochondrial Isolation and LCMS Quantification of Compound 4. On the day of experiment, 9 million RPE1 cells were treated with 20 μM DMSO or compound 4 for 2 hours and placed at 37 °C and 5% CO_2 in a humidified incubator. Mitochondria were isolated using a Qproteome Mitochondria Isolation Kit (Qiagen, catalogue no. 37612). For the LCMS quantification and analysis, an external standard curve was constructed in acetonitrile: ddH_2O, 0.001−10 μM. Standards and samples (100 μL) were mixed with acetonitrile containing warfarin and carbutamide as IS (100 μl). The extraction buffer effect was tested by mixing 50 μL of buffer and 50 μL of 1 μM standard. LC−MS/MS analysis was performed using a Waters TQs Micro coupled to an Aquity UPLC. The column was HSS T3; the mobile phase was 0.1% formic acid/acetonitrile/0.1% formic acid, with 2 min runtime at 0.5 mL/min. Calculations were performed using MassLynx and MS excel.

Downloaded from pubs.acs.org/jmcmar/article-pdf/69/20/23517/6749327/jm6c00526.pdf by UNIV OF SHEFFIELD user on 10 November 2026

https://doi.org/10.1021/acs.jmedchem.6c00526
J. Med. Chem. 2026, 69, 23517−23539

Immunofluorescence. Cells were fixed with 3.7% paraformaldehyde (PFA, Santa Cruz Biotechnology, Dallas, TX, USA) in phosphate-buffered saline (PBS) for 20 min at room temperature, at which point PFA was removed and cells were quenched with 30 mM glycine (Fisher Scientific, Hampton, NH, USA) in PBS for 5 min. Cells were permeabilized for 5 min in 0.1% Triton X-100 (Sigma) in PBS, after which samples were washed 2× in PBS, blocked in 1% BSA/PBS, and incubated for 1h at room temperature. Primary antibodies were diluted in 1% BSA/PBS, applied to samples, and incubated overnight at 4 °C. Following three 10 min washes in PBS, the secondary antibody was applied for 1 h at room temperature, protected from light. Samples for confocal microscopy were counterstained with 0.2 μg/mL Hoechst 33342 (Sigma) and washed three times for 10 min each in PBS, prior to mounting in Vectashield H-1000 on Glass slides. Images were Acquired with a Zeiss LSM 780 confocal microscope using a 40× immersion oil objective. Image analysis was performed with ImageJ (NIH) and CellProfiler (Broad Institute, Cambridge, MA, USA) software.

Super-Resolution Microscopy. Samples were prepared and immunostained as described above without Hoechst 33342 staining. STED imaging was performed with a Leica TCS SP8 STED 3× (Leica Microsystems) equipped with a HCPLAPO100×/1.40 Oil STED WHITE objective and LAS-X software. For sequential dual-color 2D STED imaging, fluorophores AF555 and AF647 were excited by a pulsed white light laser tunable from 470 to 670 nm. Optimal excitation at 550 and 640 nm was selected with STED depletion wavelengths of 660 nm and 775 nm, respectively. Emitted fluorescence was recorded on two gated detectors (HyD-SMD Leica/Hamamatsu) for imaging AF555 between 560 and 630 nm and AF647 between 650 and 720 nm. Appropriated filters were placed in front of each detector and to block STED laser background contributions (notch 660 and notch 775). Imaging of AF555 used detector gating settings of 1.0 ns with 660 nm continuous-wave depletion, and AF647 imaging used 0.5 ns with pulsed 775 nm depletion. The pinhole was set to 1 AU calculated for 580 nm emission, and the imaging pixel size was set to 23 nm with a sequential line scan speed of 200 Hz with 4 line signal averaging. All images collected are further presented as raw STED results.

Proteins and Reagents. Enzymes (APE1, UNG2, TDG, SMUG1, MPG, NEIL1, NTHL1, NUDT15, NUDT22, NUDT5) and mutants were produced as reported previously.[9,14,42,43] 8-oxoG-containing oligonucleotide (see the sequence below) was radiolabeled at the 5′ end with [γ^{32}P]-ATP (Perkin-Elmer Life Sciences) and T4 polynucleotide linase (T4PNK) from New England Biolabs.

Oligonucleotides. For PAGE analysis, oligonucleotide 5′GTA-CCCGGGGATCCGTAA**8**GCGCATCAGCTGCAG (Integrated DNA Technologies), where 8 stands for 8oxodG, was 5′-labeled and further hybridized to the complementary oligonucleotide 5′-CAG-CAGCTGATGCGCCTTACGGATCCCCGGGTAC in the presence of 60 mM Tris−HCl (pH 7.5) and 0.2 M NaCl by heating to 80 °C for 5 min before slowly cooling to room temperature overnight.

For Standard Biochemical Assay. Complementary strands containing FAM and DAB were ordered from ATD BIO. The sequences were 5′-FAM-TCTG CCA XCA CTG CGT CGA CCT G-3′ and 5′-CAG GTC GAC GCA GTG YTG GCA GT-Dab-3′, respectively, where X is a lesion such as uracil, thymine glycol, 8-oxoA, AP-site analogue, inosine, and hydroxymethyl cytosine and Y is the corresponding required complementary base.

hOGG1 Activity Assay on U:C-Containing Substrates (PAGE). To analyze the AP lyase activity of *h*OGG1 on U:C-containing substrates, 2 nM concentration of the Indicated 34 Mer [^{32}P]5′-labeled Uracil-containing substrate was incubated with 10 nM *h*OGG1 and either 10% DMSO or 6.25 μM for **5** in the presence of 30 mM Hepes, pH 7.5, 4% glycerol, and 20 mM EDTA. Samples were incubated at 37 °C for the indicated times. When specified, samples were further incubated for 10 min in the presence of 0.2 U of T4PNK. The reaction products were stabilized by incubation with 30 mM freshly prepared $NaBH_4$ and further incubation for 20 min on ice. DNA products were analyzed by 7 M Urea-20% PAGE and autoradiography.

Crystallization. Purified mOGG1 (22 mg/mL) was pre-incubated with 10 mM ligand (**4**) and crystallized via sitting drop vapor diffusion at 18 °C in condition B6 (0.09 M halogens, 0.1 M MOPS/HEPES-Na pH 7.5, 50% EDO_P8K) from the morpheus screen (molecular dimensions). Protein crystals were fished without additional cryoprotectant and flash-frozen in liquid nitrogen.

Data Collection, Structure Determination, and Refinement. X-ray diffraction data were collected at Station I03 of the diamond light source (Oxford, UK) equipped with an Eiger2 XE 16 m detector. A complete dataset was collected on a single crystal at 100 K. The dataset was processed and scaled with XDS[44] and AIMLESS[45] within the CCP4 suite.[46] Molecular replacement was performed using MOLREP[47] using the structure of mouse OGG1 (PDB ID: 6G3Y), with all ligands and waters removed, as the search model. Several rounds of manual model building and refinement were performed using COOT[48] and REFMAC5,[49] during which waters and ligands were added. The coordinates and structure factors for the mOGG1-**4** structure were deposited in the PDB database (PDB ID: 9GIH).

DSF-Based Selectivity Screening against OGG1 and a Curated Kinase Library. The assay was performed as previously described.[50,51] Briefly, protein kinase domains at a concentration of 2 μM were mixed with 10 μM compound in a buffer containing 20 mM HEPES, pH 7.5 and 500 mM NaCl. SYPRO Orange (5000×, invitrogen) was added as a fluorescence probe (1 μl per mL). Subsequently, temperature-dependent protein unfolding profiles were measured using the QuantStudio 5 Realtime PCR Machine (Thermo Fisher). Excitation and emission filters were set to 465 nm and 590 nm, respectively. The temperature was raised with a step rate of 3 °C per minute. Data points were analyzed with the Internal Software (Thermal Shift Software Version 1.4, Thermo Fisher) using the Boltzmann equation to determine the inflection point of the transition curve

Selectivity Screen against Other Glycosylases and NUDIX Enzymes. The compounds were tested at a concentration of 99 μM in biochemical assays following a similar protocol to that for the OGG1 biochemical readout, using the respective enzyme and the labeled enzyme substrate. Glycosylase inhibition was monitored in the kinetic mode and calculated in percent in relation to the DMSO control. The experiment was performed in duplicate for each compound. For NUDT5, NUDT15, and NUDT22, a malachite green assay was conducted, using a previously described protocol.[52,53]

Resazurin Cell Viability Assay with BJ-hTERT and BJ-hTERT SV40RAS Cells for Toxicity Testing in a Dose−Response Manner. Prior to cell seeding, compounds **4**, **5**, and **2** were dispensed in 384-well cell culture plates using an Echo Acoustic Liquid Handler. Dose response curves were dispensed in duplicates from 100 μM to 0.09 μM. BJ-hTERT and BJ-hTERT SV40RAS cells were cultured in DMEM Glutamax +10% FBS +50 U/50 μg/mL penicillin/streptomycin and were seeded in the cell culture plates containing the nano-dispensed compounds at concentrations of 1200 cells/well (BJ-hTERT) and 600 cells/well (BJ-hTERT SV40RAS) using a Multidrop Combi reagent dispenser. After incubation for 72 hours at 37 °C, resazurin (59 μg/mL in PBS/10 μL/well) was added, and the plates were incubated for a further 4−7 hours at 37 °C before performing a fluorescence readout on a Hidex Sense microplate reader.

Retinal Explant Model. Retinal explants were prepared as previously described.[33,34] C57BL/6 J mice (male, 3−4 months old) were euthanized by cervical dislocation, and retinas were immediately removed in cold HBSS. Retinas were flat-mounted onto cell culture inserts (Millicell 0.4 μmpore; Merck), transferred to 6-well plates containing media (Neurobasal-A media supplemented with 2 mM L-glutamate (GlutaMAX, Gibco) 2% B27, 1% N2, and 1% penicillin/streptomycin (all Gibco)). Media contained compounds at 1 or 10 μM (**4**, **5**, B) or an equivalent DMSO concentration (0.1% or 0.01%) for controls. Retinas were maintained for 3 days ex vivo (3 DEV) in a humidified incubator at 37 °C with 5% CO_2, with a half-media change (with freshly prepared compound) at 2 DEV. At 3 DEV, retinas were fixed with 3.7% PFA for 30 minutes and transferred to slides for immunolabeling. Retinas from eyes fixed immediately after

Downloaded from pubs.acs.org/jmcmar/article-pdf/69/20/23517/6749327/jm6c00526.pdf by UNIV OF SHEFFIELD user on 10 November 2026

https://doi.org/10.1021/acs.jmedchem.6c00526
J. Med. Chem. 2026, 69, 23517−23539

euthanasia were used as naïve controls. Following fixation, retinas were permeabilized with 0.5% Triton X-100 (VWR) in PBS for 1 h and blocked in 2% bovine serum albumin (BSA; Fisher Scientific) in PBS for 1 h, and Guinea-pig anti-RBPMS was applied and maintained overnight at 4 °C. Following five repeated washes of 5 min with PBS, Goat anti Guinea-pig Alexa Fluor 568 nm was applied and incubated for 4 h at room temperature. Tissue was washed as before, and the DAPI nuclear stain (1 μg/mL in PBS) was applied for 10 min. Tissue was washed once in PBS before being mounted using Fluoromount-G, and glass coverslips were applied. Slides were sealed with nail varnish. Images were acquired on a Leica DMi8 microscope with a CoolLED pE-300 white LED-based light source and a Leica DFC7000 T fluorescence color camera (all Leica). Six images per retina were taken equidistant at 0, 2, 4, 6, 8, and 10 o'clock about a superior to inferior line through the optic nerve head (~1000 μm eccentricity). Images were cropped to 100 × 100 μm, and RBPMS + cells were counted using the cell counter plugin for Fiji; counts were averaged across the 6 images. The nuclear diameter of >30 round cells per image (to exclude microglia and vascular endothelium) was measured using the line tool in FIJI, averaged per images, and averaged across the 6 images per retina.

Luminescence-Based NAD Assay. NAD assays were prepared as previously described[34] C57BL/6 J mice (male, 3-4 months old) were euthanized by cervical dislocation, and individual hemispheres of the cortex were isolated from the brain. The cortex was submerged in 800 μL of ice-cold dispase (5000 Caseinolytic units, 354235, Corning), finely chopped, and maintained on ice for transfer to the working lab (15 minutes). Sample were put on a heating block (ThermoMixer C, Eppendorf) at 37 °C, 350 rpm for 30 min before dissociation by gentle trituration. Cell concentration of the cell suspension was determined with a hemocytometer (C-Chip, NanoEntek). Samples were diluted to a concentration of 2million cells/ml with HBSS and incubated with compounds at 1 or 10 μM (**4**, **5**, B) or an equivalent DMSO concentration (0.1% or 0.01%) for 2 h at 37 °C and 5% CO_2. After incubation, samples were spun down at 7700 rpm (4000*g*) for 5 min, and the supernatant was removed and exchanged with HBSS prior to homogenization to remove the compounds. Samples were homogenized for 20 s with a handheld homogenizer (30.000 min^{-1}, VDI 12, VWR). NAD was measured using a NAD/NADHGlo kit (Promega); the NAD reagent was prepared according to the manufacturer's protocol. For each sample, 50 μL of the sample was combined with 50 μL of the reagent in a 96-well plate (Nunc F96MicroWell WhitePolystyrene plate, ThermoFisher Scientific), and luminescence was recorded with a plate reader (infinite 200, Tecan) 1 h from initial mixing. Fold changes in samples were compared to the luminescence signal in control samples.

Kinetic Solubility Assay. Performed according to enamine's aqueous solubility standard operating procedure. Briefly, using a 17.5 mM stock solution of **4** and **7** in 100% DMSO, dilutions were prepared to a theoretical concentration of 350 μM in duplicates in phosphate-buffered saline pH 7.4 (138 mM NaCl, 2.7 mM KCl, 10 mM K-phosphate) with 2% final DMSO. The experimental compound dilutions in PBS were further allowed to equilibrate at 25 °C on a Thermomixer R Block, 1.5 mL (Eppendorf, Germany; Cat # 5355) for 2 h and then filtered through HTS filter plates using a vacuum manifold. The filtrates of test compounds were diluted 2-fold with acetonitrile with 2% DMSO before measuring.

In parallel, using a 17.5 mM stock solution of **4** and **7** in 100% DMSO, dilutions were prepared to theoretical concentrations of 0 μM (blank), 8.75 μM, 21.875 μM, 43.75 μM, 87.5 μM, and 175 μM in 50% acetonitrile/PBS with 2% final DMSO to generate calibration curves. Ondansetron was used as a reference compound to control proper assay performance. 200 μL of each sample was transferred to a 96-well plate and measured in the 230−550 nm range with a 5 nm step on a SpectraMax Paradigm Reader (Multi-Mode Detection Platform, Product # 33270−1279) using SoftMax Pro v.5.4 (Molecular Devices) software.

The concentrations of compounds in the PBS filtrate were calculated using a dedicated Microsoft Excel calculation script. Proper absorbance wavelengths for calculations were selected for each compound manually based on absorbance maxima (absolute absorbance unit values for the minimum and maximum concentration points within the 0−3 OD range). Each final data set was visually evaluated by the operator, and goodness-of-fit (R^2) was calculated for each calibration curve. The effective range of this assay was approximately 2−350 μM, and the compounds returning values close to the upper limit of the range may have higher actual solubility (e.g., 5′-deoxy-5-fluorouridine).

Microsomal Stability Assay. Microsomal incubations were carried out in 96-well plates in 5 aliquots of 30 μL each (one for each time point. Liver microsomal incubation medium comprised of phosphate buffer (100 mM, pH 7.4), $MgCl_2$ (3.3 mM), NADPH (3 mM), glucose-6-phosphate (5.3 mM), and glucose-6-phosphate dehydrogenase (0.67 units/mL) with 0.42 mg of liver microsomal protein per mL. In the control reactions, the NADPH-cofactor system was substituted with phosphate buffer. Test compounds (2 μM, final acetonitrile concentration 1.6%) were incubated with microsomes at 37 °C, shaking at 100 rpm in a Shaker Innova 4330 (New Brunswick Scientific). Five time points over 40 min were analyzed. The reactions were stopped by adding 5 volumes of acetonitrile with the internal standard to incubation aliquots, followed by protein sedimentation by centrifuging at 5500 rpm for 5 min. Each reaction was performed in duplicate. Supernatants were analyzed using a gradient HPLC system (Agilent Technologies) coupled to a triple quadrupole mass-detector API 3000 with a TurboIonSpray Ion Source (AB Sciex, Canada). The elimination rate constant (k_{el}), half-life ($t_{1/2}$), and intrinsic clearance (Cl_{int}) were determined in a plot of ln(AUC) versus time, using linear regression analysis.

Caco-2 Permeability Assay. Caco-2 cells were cultured in 75 mL flasks to 80−90% confluence according to the ATCC and millipore recommendations in a humidified atmosphere at 37 °C and 5% CO_2. Cells were detached with trypsin/EDTA solution, resuspended in the complete medium containing DMEM high-glucose (4500 mg/L) with L-glutamine (4 mM) supplemented with 10% heat-inactivated fetal bovine serum, 1% nonessential amino acids, and 730 nM puromycin, and seeded at a density of 5 × 10^5 cells in a 75 mL flask. After 5 days, cells were trypsinized and resuspended in the complete medium to a final concentration of 600 × 103 cells/mL; 400 μL of the cell suspension was added to each well of the HTS 24-Multiwell Insert System, and 25 mL of prewarmed complete medium was added to the feeder tray. Caco-2 cells were incubated in a Multiwell Insert System for 6−10 days before the transport experiments. The medium in the filter plate and feeder tray was refreshed every other day. Prior to the transport experiment, the integrity of the monolayer was verified by measuring the transepithelial electrical resistance (TEER) for every well using the Millicell-ERS system Ohm meter. The final TEER values were within the range of 150−600 Ω × cm^2, as required for the assay conditions. The 24-well insert plate was removed from its feeder plate and placed in a new sterile 24-well transport analysis plate. The inserts were washed with PBS after medium aspiration. Ketoprofen, atenolol, and Digoxin were used as reference compounds.

To determine the rate of compound transport in apical (A)-to-basolateral (B) direction, 300 μL of the test compound dissolved in transport buffer (Hanks' BSS (9.5 g/L) and $NaHCO_3$ (0.35 g/L) with $MgSO_4$ to a final concentration of 0.81 mM, $CaCl_2$ to a final concentration of 1.26 mM, and HEPES to a final concentration of 25 mM. pH adjusted to 7.4 was added into the filter wells; 1000 μL of transport buffer was added to transport analysis plate wells.

To determine transport rates in the basolateral (B)-to-apical (A) direction, 1000 μL of the test compound solutions was added into the wells of the transport analysis plate; the wells in the filter plate were filled with 300 μL of buffer (apical compartment).

The effect of the inhibitor on the P-gp-mediated transport of the tested compounds was assessed by determining the bidirectional transport in the presence or absence of verapamil. The Caco-2 cells were preincubated for 30 min at 37 °C with 100 μM verapamil in both apical and basolateral compartments. After removal of the pre-incubation medium, the test compounds with verapamil (100 μM) in transport buffer were added to donor wells, while the receiver wells were filled with the appropriate volume of transport buffer with 100 μM

Downloaded from pubs.acs.org/jmcmar/article-pdf/69/20/23517/6749327/jm6c00526.pdf by UNIV OF SHEFFIELD user on 10 November 2026

https://doi.org/10.1021/acs.jmedchem.6c00526
J. Med. Chem. 2026, 69, 23517−23539

verapamil. The final amount of test and reference compounds was 10 μM.

The plates were incubated for 90 min at 37 °C under continuous shaking at 100 rpm. 75 μL aliquots were taken from the donor and receiver compartments for LC−MS/MS analysis. All samples were mixed with 2 volumes of acetonitrile, followed by protein sedimentation by centrifuging at 10000 rpm for 10 min. Supernatants were analyzed using the HPLC system coupled with a tandem mass spectrometer.

All solutions of test and reference compounds were prepared manually, and further manipulations with the solutions were performed with automation using Opentrons. The apparent permeability (P_{app}) was calculated for the Caco-2 permeability assay using the following equation

$$P_{app} = \frac{V_A}{\text{Area} \times \text{Time}} \times \frac{[\text{drug}]_{acc}}{[\text{drug}]_{initial,\,d}}$$

where V_A is the volume of transport buffer in the acceptor well, Area is the surface area of the inset (equal to the effective growth area of the inset—0.7 cm^2), *Time* is the time of the assay, $[\text{drug}]_{acc}$ is the amount of the test compound in an acceptor well, and $[\text{drug}]_{initial,\,d}$ is the initial amount of the test compound in a donor well.

Efflux ratio (P_{app}(BA)/P_{app}(AB)) reveals the difference in P_{app} as a result of active transport. If the efflux ratio is greater than 2, this indicates the occurred active efflux.

Statistics. Unless stated otherwise, all biochemical assays were performed in three independent replicates, with triplicates in each experiment. In cell biology experiments, each bar represents the mean ± SD or mean ± SED. Data are the average of three biological replicates. In the biological experiments, statistical significance was calculated using one-way ANOVA coupled with a Tukey test for multiple comparisons; ns, non-significant; *$P < P < 0.05$; **$P < 0.01$; ***$P < 0.001$; ****$P < 0.0001$.

■ ASSOCIATED CONTENT

Supporting Information

The Supporting Information is available free of charge at https://pubs.acs.org/doi/10.1021/acs.jmedchem.6c00526.

Additional experimental data, including cellular assays, mitochondrial localization and mtDNA damage analyses, compound toxicity and selectivity profiling, calculated pKa values, crystallographic data and refinement statistics, and NMR and mass spectrometry data (PDF)

Molecular Formula Strings and the associated biochemical and biological data (CSV)

Accession Codes

The atomic coordinates and structure factors for the OGG1−compound **4** complex have been deposited in the Protein Data Bank under accession code 9GIH. Authors will release the atomic coordinates upon article publication.

■ AUTHOR INFORMATION

Corresponding Authors

Maeve Long − *Science for Life Laboratory, Department of Oncology-Pathology, Karolinska Institutet, 17165 Solna, Sweden;* Email: longmaeve123@gmail.com

Maurice Michel − *Science for Life Laboratory, Department of Oncology-Pathology, Karolinska Institutet, 17165 Solna, Sweden; Center for Molecular Medicine, Department of Oncology-Pathology, Karolinska Institute and Karolinska Hospital, 17176 Stockholm, Sweden;* orcid.org/0000-0003-3261-2493; Emai: maurice.michel@ki.se

Authors

James Tribble − *Division of Eye and Vision, Department of Clinical Neuroscience, St. Erik Eye Hospital, Karolinska Institutet, 17164 Stockholm, Sweden; Wolfson Sensory, Pain and Regeneration Centre (SPaRC), School of Neuroscience, Guy's Campus, King's College London, London SE1 1UL, U.K.*

Rahul Upadhyay − *Science for Life Laboratory, Department of Oncology-Pathology, Karolinska Institutet, 17165 Solna, Sweden; Center for Molecular Medicine, Department of Oncology-Pathology, Karolinska Institute and Karolinska Hospital, 17176 Stockholm, Sweden*

Alice Eddershaw − *Center for Molecular Medicine, Department of Oncology-Pathology, Karolinska Institute and Karolinska Hospital, 17176 Stockholm, Sweden;* orcid.org/0000-0002-8381-4135

Nicholas D. D'Arcy-Evans − *Science for Life Laboratory, Department of Oncology-Pathology, Karolinska Institutet, 17165 Solna, Sweden*

Alan Nicol − *Division of Eye and Vision, Department of Clinical Neuroscience, St. Erik Eye Hospital, Karolinska Institutet, 17164 Stockholm, Sweden*

Sara Cano − *Medical Faculty, Institute of Biochemistry II, Goethe University Frankfurt, 60590 Frankfurt am Main, Germany; Buchmann Institute for Molecular Lifesciences, Goethe University Frankfurt, 60438 Frankfurt am Main, Germany*

Emma Scaletti Hutchinson − *Department of Biochemistry and Biophysics, Stockholm University, 10405 Stockholm, Sweden;* orcid.org/0000-0002-8741-8981

Alicia del Prado − *Centro de Biología Molecular Severo Ochoa (CSIC-UAM), 28049 Madrid, Spain*

Hannah Stigsdotter − *Science for Life Laboratory, Department of Oncology-Pathology, Karolinska Institutet, 17165 Solna, Sweden*

Natálie Rudolfová − *Center for Molecular Medicine, Department of Oncology-Pathology, Karolinska Institute and Karolinska Hospital, 17176 Stockholm, Sweden*

Dinesh Nirmalan − *Center for Molecular Medicine, Department of Oncology-Pathology, Karolinska Institute and Karolinska Hospital, 17176 Stockholm, Sweden*

Elisée Wiita − *Science for Life Laboratory, Department of Oncology-Pathology, Karolinska Institutet, 17165 Solna, Sweden*

Ingrid Almlöf − *Science for Life Laboratory, Department of Oncology-Pathology, Karolinska Institutet, 17165 Solna, Sweden*

Richard Svensson − *Department of Pharmacy, Uppsala Drug Optimization and Pharmaceutical Profiling (UDOPP), Uppsala University, 75123 Uppsala, Sweden*

Andreas Krämer − *Department of Pharmacy, SciLifeLab Drug Discovery and Development Platform, Uppsala University, 75123 Uppsala, Sweden*

Anas Bitar − *Institute of Pharmaceutical Chemistry & Structural Genomics Consortium (SGC), Goethe University, 60438 Frankfurt, Germany; Department of Pathology, Duke University School of Medicine, Durham, North Carolina 27710, United States; Duke Center for Neurodegeneration and Neurotherapeutics, Durham, North Carolina 27710, United States;* orcid.org/0000-0001-7687-5055

Downloaded from pubs.acs.org/jmcmar/article-pdf/69/20/23517/6749327/jm6c00526.pdf by UNIV OF SHEFFIELD user on 10 November 2026

Oryn Purewal-Sidhu − *Science for Life Laboratory, Department of Oncology-Pathology, Karolinska Institutet, 17165 Solna, Sweden*
Oliver Mortusewicz − *Science for Life Laboratory, Department of Oncology-Pathology, Karolinska Institutet, 17165 Solna, Sweden*
Olov Wallner − *Science for Life Laboratory, Department of Oncology-Pathology, Karolinska Institutet, 17165 Solna, Sweden*
Opher Gileadi − *Center for Molecular Medicine, Structural Genomics Consortium, Department of Medicine Solna, Karolinska Institutet and Karolinska Hospital, 17176 Stockholm, Sweden*
Evert J. Homan − *Science for Life Laboratory, Department of Oncology-Pathology, Karolinska Institutet, 17165 Solna, Sweden*
Stefan Knapp − *Department of Pharmacy, SciLifeLab Drug Discovery and Development Platform, Uppsala University, 75123 Uppsala, Sweden*
Pawel Baranczewski − *Department of Pharmacy, Uppsala Drug Optimization and Pharmaceutical Profiling (UDOPP), Uppsala University, 75123 Uppsala, Sweden*
Laurie H. Sanders − *Institute of Pharmaceutical Chemistry & Structural Genomics Consortium (SGC), Goethe University, 60438 Frankfurt, Germany; Department of Pathology, Duke University School of Medicine, Durham, North Carolina 27710, United States; Duke Center for Neurodegeneration and Neurotherapeutics, Durham, North Carolina 27710, United States*
Miguel de Vega − *Centro de Biología Molecular Severo Ochoa (CSIC-UAM), 28049 Madrid, Spain;* orcid.org/0000-0003-1285-7549
Pål Stenmark − *Department of Biochemistry and Biophysics, Stockholm University, 10405 Stockholm, Sweden;* orcid.org/0000-0003-4777-3417
Alexandra Stolz − *Medical Faculty, Institute of Biochemistry II, Goethe University Frankfurt, 60590 Frankfurt am Main, Germany; Buchmann Institute for Molecular Lifesciences, Goethe University Frankfurt, 60438 Frankfurt am Main, Germany*
Thomas Helleday − *Science for Life Laboratory, Department of Oncology-Pathology, Karolinska Institutet, 17165 Solna, Sweden; Weston Park Cancer Centre, Department of Oncology and Metabolism, The Medical School, University of Sheffield, Sheffield S10 2SJ, U.K.*
Michael Sundström − *Department of Neurology, Duke University School of Medicine, Durham, North Carolina 27710, United States*
Pete Williams − *Division of Eye and Vision, Department of Clinical Neuroscience, St. Erik Eye Hospital, Karolinska Institutet, 17164 Stockholm, Sweden; Centre for Eye Research Australia, Royal Victorian Eye and Ear Hospital, 3002 Melbourne, Australia;* orcid.org/0000-0001-6194-8397

Complete contact information is available at: https://pubs.acs.org/doi/10.1021/acs.jmedchem.6c00526

Author Contributions

CRediT: All authors have given approval to the final version of the manuscript. Conceptualization: M.L., M.M.; Methodology: M.L., P.S., A.S., P.W., M.M.; Software: E.S.H., E.H.; Validation: M.L., J.T., R.U., A.E., N.D.D.A., S.C., E.S.H., A.B., R.S., A.D.P., H.S., N.R., D.N., E.W., I.A., A.K., O.W., O.G., E.J.H., M.D.V., M.M.; Formal analysis: M.L., H.T., R.U., A.E., E.S.H., A.d.P., E.W., A.B., R.S., I.A., O.W., E.J.H., M.d.V., M.M.; Investigation: M.L., J.T., R.U., A.E., N.D.D.A., S.C.F., E.S.H., O.P.S., A.d.P., H.S., A.B., R.S., N.R., D.N., E.W., I.A., A.K., O.W., M.d.V., M.M.; Resources: S.K., M.d.V., P.S., T.H., M.S., A.S., P.B., L.H.S., P.W., M.M.; Data Curation: E.J.H., O.W., M.M.; Writing—Original Draft: M.L., J.T., R.U., A.E., E.S.H., M.M.; Writing—Review and Editing: M.L., J.T., R.U., P.W., M.M.; Visualization: M.L., J.T., R.U., A.E., E.S.H., A.d.P., M.M.; Supervision: O.M., O.W., O.G., E.J.H., S.K., P.B., L.H.S., M.d.V., P.S., A.S., P.W., M.M.; Project administration: M.M.; Funding acquisition: M.L., S.K., M.d.V., P.S., T.H., L.H.S., M.S., A.S., P.W., M.M.

Funding

This work was funded by the Åke-Olsson foundation for haematological research (2020-00306, MM and ML), the Helleday Foundation and Barncancerfonden Postdoctoral Grant (ML), a Novo Nordisk Pioneer Innovator Grant (NNF23OC0085944, MM), the Åke Wiberg Foundation (M23−0043, MM), and the Maximon Longevity Foundation (MM) and Karolinska Institute Research Foundation Grant (2022-01776, MM). PW is supported by Vetenskapsrådet 2022-00799. TH is supported by Swedish Research Council (2015-00162) and the Swedish Childhood Cancer Foundation (PR2021-0030). PS was supported by grants from the Swedish Cancer Society (24 3848 Pj) and the Swedish Research Council (2022-03681). LHS was supported by an NIH grant R01NS119528. This project has received funding from the Innovative Medicines Initiative 2 Joint Undertaking (JU) under grant agreement No 875510 (M.M., E.J.H., E.W., I.A., M.L., O.W., O.M., R.U., O.G., A.S., S.K., M.S., D.N., A.K., S.C., A.E., N.R). The JU receives support from the European Union's Horizon 2020 research and innovation programme and EFPIA and Ontario Institute for Cancer Research, Royal Institution for the Advancement of Learning McGill University, Kungliga Tekniska Högskolan, Diamond Light Source Limited. This communication reflects the views of the authors and the JU is not liable for any use that may be made of the information contained herein.

Notes

All animal procedures were undertaken in accordance with the Association for Research in Vision and Ophthalmology (ARVO) Statement for the Use of Animals in Ophthalmic and Vision Researc. The experimental procedures involving mice were approved by Stockholm's Committee for Ethical Animal Research (approval no. 10389-2018).

The authors declare the following competing financial interest(s): MM is consultant to Novartis. All remaining authors have no conflict of interest to report.

■ ACKNOWLEDGMENTS

We thank the taxpayers of our individual countries for their generous support of our research. We thank the imaging facility at Scilifelab for their support with the super-resolution microscopy imaging, specifically Hans Blom. We are thankful to Athina Pliakou, Mari Kullman Magnusson, Kristina Edfeldt, Pontus Petersson, and Ivan Vilotijević for administrative support. We thank the beamline scientists at station I03 of the

Downloaded from pubs.acs.org/jmcmar/article-pdf/69/20/23517/6749327/jm6c00526.pdf by UNIV OF SHEFFIELD user on 10 November 2026

Diamond Light Source (Oxford, UK) for their support during X-ray diffraction data collection.

■ ABBREVIATIONS

8oxoG, 8oxoguanine; APE1, apurinic/apyrimidinic endonuclease 1; AP site, Apurinic site; BER, base excision repair; BJ TERT, BJ (cell line name) human telomerase reverse transcriptase; CRISPR Cas9, clustered regularly interspaced short palindromic repeats CRISPR-associated protein 9; DMAP, 4-dimethyl-amino-pyridine; DMSO, dimethyl sulfoxide; DNA, deoxyribonucleic acid; MMP, mitochondrial membrane potential; mtDNA, mitochondrial DNA; NAD+, nicotinamide adenine dinucleotide; NUDIX, nucleoside diphosphate attached to sequence X; OGG1, 8-oxoguanine DNA glycosylase 1; ORCA, organocatalytic switch; PQ, paraquat; ROS, reactive oxygen species; SMUG1, single-strand selective monofunctional uracil DNA glycosylase; TDG, thymine-DNA glycosylase; TMRM, tetramethylrhodamine, methyl ester, perchlorate; UNG, Uracil-DNA glycosylase.

■ REFERENCES

(1) López-Otín, C.; Blasco, M. A.; Partridge, L.; Serrano, M.; Kroemer, G. Hallmarks of Aging: An Expanding Universe. *Cell* **2023**, *186* (2), 243−278.
(2) Pan, L.; Zhu, B.; Hao, W.; Zeng, X.; Vlahopoulos, S. A.; Hazra, T. K.; Hegde, M. L.; Radak, Z.; Bacsi, A.; Brasier, A. R.; Ba, X.; Boldogh, I. Oxidized Guanine Base Lesions Function in 8-Oxoguanine DNA Glycosylase-1-Mediated Epigenetic Regulation of Nuclear Factor κB-Driven Gene Expression. *J. Biol. Chem.* **2016**, *291* (49), 25553−25566.
(3) Ding, Y.; Fleming, A. M.; Burrows, C. J. Sequencing the Mouse Genome for the Oxidatively Modified Base 8-Oxo-7,8-Dihydroguanine by OG-Seq. *J. Am. Chem. Soc.* **2017**, *139* (7), 2569−2572.
(4) Lia, D.; Reyes, A.; de Melo Campos, J. T. A.; Piolot, T.; Baijer, J.; Radicella, J. P.; Campalans, A. Mitochondrial Maintenance under Oxidative Stress Depends on Mitochondrially Localised α-OGG1. *J. Cell Sci.* **2018**, *131* (12), jcs213538.
(5) de Souza-Pinto, N. C.; Eide, L.; Hogue, B. A.; Thybo, T.; Stevnsner, T.; Seeberg, E.; Klungland, A.; Bohr, V. A. Repair of 8-Oxodeoxyguanosine Lesions in Mitochondrial Dna Depends on the Oxoguanine Dna Glycosylase (OGG1) Gene and 8-Oxoguanine Accumulates in the Mitochondrial Dna of OGG1-Defective Mice. *Cancer Res.* **2001**, *61* (14), 5378−5381.
(6) Boldogh, I.; Hajas, G.; Aguilera-Aguirre, L.; Hegde, M. L.; Radak, Z.; Bacsi, A.; Sur, S.; Hazra, T. K.; Mitra, S. Activation of Ras Signaling Pathway by 8-Oxoguanine DNA Glycosylase Bound to Its Excision Product, 8-Oxoguanine. *J. Biol. Chem.* **2012**, *287* (25), 20769−20773.
(7) Fleming, A. M.; Ding, Y.; Burrows, C. J. Oxidative DNA Damage Is Epigenetic by Regulating Gene Transcription via Base Excision Repair. *Proc. Natl. Acad. Sci. U.S.A.* **2017**, *114* (10), 2604−2609.
(8) Ba, X.; Bacsi, A.; Luo, J.; Aguilera-Aguirre, L.; Zeng, X.; Radak, Z.; Brasier, A. R.; Boldogh, I. 8-Oxoguanine DNA Glycosylase-1 Augments Proinflammatory Gene Expression by Facilitating the Recruitment of Site-Specific Transcription Factors. *The Journal of Immunology* **2014**, *192* (5), 2384−2394.
(9) Visnes, T.; Cázares-Körner, A.; Hao, W.; Wallner, O.; Masuyer, G.; Loseva, O.; Mortusewicz, O.; Wiita, E.; Sarno, A.; Manoilov, A.; Astorga-Wells, J.; Jemth, A.-S.; Pan, L.; Sanjiv, K.; Karsten, S.; Gokturk, C.; Grube, M.; Homan, E. J.; Hanna, B. M. F.; Paulin, C. B. J.; Pham, T.; Rasti, A.; Berglund, U. W.; von Nicolai, C.; Benitez-Buelga, C.; Koolmeister, T.; Ivanic, D.; Iliev, P.; Scobie, M.; Krokan, H. E.; Baranczewski, P.; Artursson, P.; Altun, M.; Jensen, A. J.; Kalderén, C.; Ba, X.; Zubarev, R. A.; Stenmark, P.; Boldogh, I.; Helleday, T. Small-Molecule Inhibitor of OGG1 Suppresses Proinflammatory Gene Expression and Inflammation. *Science* **2018**, *362* (6416), 834−839.
(10) Komakula, S. S. B.; Tumova, J.; Kumaraswamy, D.; Burchat, N.; Vartanian, V.; Ye, H.; Dobrzyn, A.; Lloyd, R. S.; Sampath, H. The DNA Repair Protein OGG1 Protects Against Obesity by Altering Mitochondrial Energetics in White Adipose Tissue. *Sci Rep* **2018**, *8* (1), 14886.
(11) Komakula, S. S. B.; Blaze, B.; Ye, H.; Dobrzyn, A.; Sampath, H. A Novel Role for the DNA Repair Enzyme 8-Oxoguanine DNA Glycosylase in Adipogenesis. *Int. J. Mol. Sci.* **2021**, *22* (3), 1152.
(12) Hussain, M.; Chu, X.; Duan Sahbaz, B.; Gray, S.; Pekhale, K.; Park, J.-H.; Croteau, D. L.; Bohr, V. A. Mitochondrial OGG1 Expression Reduces Age-Associated Neuroinflammation by Regulating Cytosolic Mitochondrial DNA. *Free Radic Biol Med* **2023**, *203*, 34−44.
(13) Li, M.; Wang, Y.; Li, S.; Wei, Y.; Wang, G.; Du, E.; Huang, Z.; Zhang, B.; Tao, Y.; Song, Z. OGG1 Modulates the Crosstalk of Microglia and Müller Cells in Degenerative Retinas via Alleviating Inflammatory Response and Oxidative Stress. *Exp. Eye Res.* **2026**, *262*, 110695.
(14) Michel, M.; Benítez-Buelga, C.; Calvo, P. A.; Hanna, B. M. F.; Mortusewicz, O.; Masuyer, G.; Davies, J.; Wallner, O.; Sanjiv, K.; Albers, J. J.; Castañeda-Zegarra, S.; Jemth, A.-S.; Visnes, T.; Sastre-Perona, A.; Danda, A. N.; Homan, E. J.; Marimuthu, K.; Zhenjun, Z.; Chi, C. N.; Sarno, A.; Wiita, E.; von Nicolai, C.; Komor, A. J.; Rajagopal, V.; Müller, S.; Hank, E. C.; Varga, M.; Scaletti, E. R.; Pandey, M.; Karsten, S.; Haslene-Hox, H.; Loevenich, S.; Marttila, P.; Rasti, A.; Mamonov, K.; Ortis, F.; Schömberg, F.; Loseva, O.; Stewart, J.; D'Arcy-Evans, N.; Koolmeister, T.; Henriksson, M.; Michel, D.; de Ory, A.; Acero, L.; Calvete, O.; Scobie, M.; Hertweck, C.; Vilotijevic, I.; Kalderén, C.; Osorio, A.; Perona, R.; Stolz, A.; Stenmark, P.; Berglund, U. W.; de Vega, M.; Helleday, T. Small-Molecule Activation of OGG1 Increases Oxidative DNA Damage Repair by Gaining a New Function. *Science* **2022**, *376* (6600), 1471−1476.
(15) Youhanna, S.; Kemas, A. M.; Wright, S. C.; Zhong, Y.; Klumpp, B.; Klein, K.; Motso, A.; Michel, M.; Ziegler, N.; Shang, M.; Sabatier, P.; Kannt, A.; Sheng, H.; Oliva-Vilarnau, N.; Büttner, F. A.; Seashore-Ludlow, B.; Schreiner, J.; Windbergs, M.; Cornillet, M.; Björkström, N. K.; Hülsmeier, A. J.; Hornemann, T.; Olsen, J. V.; Wang, Y.; Gramignoli, R.; Sundström, M.; Lauschke, V. M. Chemogenomic Screening in a Patient-Derived 3D Fatty Liver Disease Model Reveals the CHRM1-TRPM8 Axis as a Novel Module for Targeted Intervention. *Adv. Sci.* **2024**, *12*, 2407572.
(16) Kehler, M.; Zhou, K.; Kemas, A. M.; Del Prado, A.; Hutchinson, E. S.; Nairn, E. H.; Varga, M.; Plattner, Y.; Zhong, Y.; Purewal-Sidhu, O.; Haslam, J.; Wiita, E.; Gildie, H.; Singerova, K.; Szaruga, Z.; Almlöf, I.; Hormann, F. M.; Liu, K.-C.; Wallner, O.; Ortis, F.; Homan, E. J.; Gileadi, O.; Rudd, S. G.; Stenmark, P.; De Vega, M.; Helleday, T.; D'Arcy-Evans, N. D.; Lauschke, V. M.; Michel, M. Organocatalytic Switches of DNA Glycosylase OGG1 Catalyze a Highly Efficient AP-lyase Function. *Chem. A Eur. J* **2025**, *31*, e202500382.
(17) Visnes, T.; Benitez-Buelga, C.; Cázares-Körner, A.; Sanjiv, K.; Hanna, B. M. F.; Mortusewicz, O.; Rajagopal, V.; Albers, J. J.; Hagey, D. W.; Bekkhus, T.; Eshtad, S.; Baquero, J. M.; Masuyer, G.; Wallner, O.; Müller, S.; Pham, T.; Göktürk, C.; Rasti, A.; Suman, S.; Torres-Ruiz, R.; Sarno, A.; Wiita, E.; Homan, E. J.; Karsten, S.; Marimuthu, K.; Michel, M.; Koolmeister, T.; Scobie, M.; Loseva, O.; Almlöf, I.; Unterlass, J. E.; Pettke, A.; Boström, J.; Pandey, M.; Gad, H.; Herr, P.; Jemth, A.-S.; El Andaloussi, S.; Kalderén, C.; Rodriguez-Perales, S.; Benitez, J.; Krokan, H. E.; Altun, M.; Stenmark, P.; Berglund, U. W.; Helleday, T. Targeting OGG1 Arrests Cancer Cell Proliferation by Inducing Replication Stress. *Nucleic Acids Res.* **2020**, *48* (21), 12234−12251.
(18) Tahara, Y.; Auld, D.; Ji, D.; Beharry, A. A.; Kietrys, A. M.; Wilson, D. L.; Jimenez, M.; King, D.; Nguyen, Z.; Kool, E. T. Potent and Selective Inhibitors of 8-Oxoguanine DNA Glycosylase. *J. Am. Chem. Soc.* **2018**, *140* (6), 2105−2114.
(19) Baptiste, B. A.; Katchur, S. R.; Fivenson, E. M.; Croteau, D. L.; Rumsey, W. L.; Bohr, V. A. Enhanced Mitochondrial DNA Repair of the Common Disease-Associated Variant, Ser326Cys, of hOGG1 through Small Molecule Intervention. *Free Radical Biology and Medicine* **2018**, *124*, 149−162.

Downloaded from pubs.acs.org/jmcmar/article-pdf/69/20/23517/6749327/jm6c00526.pdf by UNIV OF SHEFFIELD user on 10 November 2026

(20) Hank, E. C.; D'Arcy-Evans, N. D.; Scaletti, E. R.; Benítez-Buelga, C.; Wallner, O.; Ortis, F.; Zhou, K.; Meng, L.; Del Prado, A.; Calvo, P.; Almlöf, I.; Wiita, E.; Nierlin, K.; Košenina, S.; Krämer, A.; Eddershaw, A.; Kehler, M.; Long, M.; Jemth, A.-S.; Dawson, H.; Stewart, J.; Dickey, A.; Astorga, M. E.; Varga, M.; Homan, E. J.; Scobie, M.; Knapp, S.; Sastre, L.; Stenmark, P.; De Vega, M.; Helleday, T.; Michel, M. Nucleobase Catalysts for the Enzymatic Activation of 8-Oxoguanine DNA Glycosylase 1. *RSC Chem. Biol.* **2026**, *7* (1), 169−181.
(21) Tian, G.; Katchur, S. R.; Jiang, Y.; Briand, J.; Schaber, M.; Kreatsoulas, C.; Schwartz, B.; Thrall, S.; Davis, A. M.; Duvall, S.; Kaufman, B. A.; Rumsey, W. L. Small Molecule-Mediated Allosteric Activation of the Base Excision Repair Enzyme 8-Oxoguanine DNA Glycosylase and Its Impact on Mitochondrial Function. *Sci Rep.* **2022**, *12* (1), 14685.
(22) Visnes, T.; Zhou, K.; Kemas, A. M.; Campopiano, D.; Lauschke, V. M.; Michel, M. Chemical Switching: A Concept Inspired by Strategies from Biocatalysis and Organocatalysis. *ChemBioChem* **2025**, *26* (11), e202500220.
(23) Varga, M.; Ortis, F.; Del Prado, A.; Eddershaw, A.; Scaletti Hutchinson, E.; Hank, E. C.; Zhou, K.; Rudolfová, N.; Dodaro, A.; Wiita, E.; Almlöf, I.; Karsten, S.; Mamonov, K.; Ahmed, S. H.; Bentley, K.; Wallner, O.; Homan, E. J.; Scobie, M.; Helleday, T.; Prejanò, M.; Stenmark, P.; De Vega, M.; Watson, A. J. B.; Michel, M. Giving an Enzyme Scissors: Serotonin Derivatives as Potent Organocatalytic Switches for DNA Repair Enzyme OGG1. *J. Med. Chem.* **2025**, *68*, 22455−22483.
(24) Saul, D.; Lischer, C.; Bruns, H.; Ziegler, N.; Kannt, A.; Michel, M.; Mougiakakos, D. OGG1 Activation Improves T Cell Resilience to Oxidative Stress after Allo-SCT and T Cell Engager Exposure. *Leukemia* **2025**, *39*, 3037−3041.
(25) Michel, M.; Taebnia, N.; Lauschke, V. M. Facilitated DNA Damage Repair as an Emerging Therapeutic Strategy for Inflammatory and Fibrotic Diseases. *RSC Chem. Biol.* **2026**, *7*, 796−809.
(26) Huang, T.; Zhang, T.; Gao, J. Targeted Mitochondrial Delivery: A Therapeutic New Era for Disease Treatment. *J. Controlled Release* **2022**, *343*, 89−106.
(27) Pan, X.; Wang, H.; Li, C.; Zhang, J. Z. H.; Ji, C. MolGpka: A Web Server for Small Molecule p K_a Prediction Using a Graph-Convolutional Neural Network. *J. Chem. Inf. Model.* **2021**, *61* (7), 3159−3165.
(28) Rumsey, W. L.; Bolognese, B.; Davis, A. B.; Flamberg, P. L.; Foley, J. P.; Katchur, S. R.; Kotzer, C. J.; Osborn, R. R.; Podolin, P. L. Effects of Airborne Toxicants on Pulmonary Function and Mitochondrial DNA Damage in Rodent Lungs. *MUTAGE* **2016**, gew063.
(29) Cochemé, H. M.; Murphy, M. P. Complex I Is the Major Site of Mitochondrial Superoxide Production by Paraquat. *J. Biol. Chem.* **2008**, *283* (4), 1786−1798.
(30) Tyugashev, T. E.; Vorobjev, Y. N.; Kuznetsova, A. A.; Lukina, M. V.; Kuznetsov, N. A.; Fedorova, O. S. Roles of Active-Site Amino Acid Residues in Specific Recognition of DNA Lesions by Human 8-Oxoguanine-DNA Glycosylase (OGG1). *J. Phys. Chem. B* **2019**, *123* (23), 4878−4887.
(31) Kaur, M. P.; Guggenheim, E. J.; Pulisciano, C.; Akbar, S.; Kershaw, R. M.; Hodges, N. J. Cellular Accumulation of Cys326-OGG1 Protein Complexes under Conditions of Oxidative Stress. *Biochem. Biophys. Res. Commun.* **2014**, *447* (1), 12−18.
(32) Qi, R.; Sammler, E.; Gonzalez-Hunt, C. P.; Barraza, I.; Pena, N.; Rouanet, J. P.; Naaldijk, Y.; Goodson, S.; Fuzzati, M.; Blandini, F.; Erickson, K. I.; Weinstein, A. M.; Lutz, M. W.; Kwok, J. B.; Halliday, G. M.; Dzamko, N.; Padmanabhan, S.; Alcalay, R. N.; Waters, C.; Hogarth, P.; Simuni, T.; Smith, D.; Marras, C.; Tonelli, F.; Alessi, D. R.; West, A. B.; Shiva, S.; Hilfiker, S.; Sanders, L. H. A Blood-Based Marker of Mitochondrial DNA Damage in Parkinson's Disease. *Sci. Transl. Med.* **2023**, *15* (711), eabo1557.
(33) Xu, X.; Pang, Y.; Fan, X. Mitochondria in Oxidative Stress, Inflammation and Aging: From Mechanisms to Therapeutic Advances. *Sig Transduct Target Ther* **2025**, *10* (1), 190.
(34) Brown, O. R.; Heitkamp, M.; Song, C.-S. Niacin Reduces Paraquat Toxicity in Rats. *Science* **1981**, *212* (4502), 1510−1512.
(35) Tribble, J. R.; Otmani, A.; Sun, S.; Ellis, S. A.; Cimaglia, G.; Vohra, R.; Jöe, M.; Lardner, E.; Venkataraman, A. P.; Dominguez-Vicent, A.; Kokkali, E.; Rho, S.; Jóhannesson, G.; Burgess, R. W.; Fuerst, P. G.; Brautaset, R.; Kolko, M.; Morgan, J. E.; Crowston, J. G.; Votruba, M.; Williams, P. A. Nicotinamide Provides Neuroprotection in Glaucoma by Protecting against Mitochondrial and Metabolic Dysfunction. *Redox Biol.* **2021**, *43*, 101988.
(36) Tribble, J. R.; Jöe, M.; Varricchio, C.; Otmani, A.; Canovai, A.; Habchi, B.; Daskalakis, E.; Chaleckis, R.; Loreto, A.; Gilley, J.; Wheelock, C. E.; Jóhannesson, G.; Wong, R. C. B.; Coleman, M. P.; Brancale, A.; Williams, P. A. NMNAT2 Is a Druggable Target to Drive Neuronal NAD Production. *Nat. Commun.* **2024**, *15* (1), 6256.
(37) Loreto, A.; Hill, C. S.; Hewitt, V. L.; Orsomando, G.; Angeletti, C.; Gilley, J.; Lucci, C.; Sanchez-Martinez, A.; Whitworth, A. J.; Conforti, L.; Dajas-Bailador, F.; Coleman, M. P. Mitochondrial Impairment Activates the Wallerian Pathway through Depletion of NMNAT2 Leading to SARM1-Dependent Axon Degeneration. *Neurobiol. Dis.* **2020**, *134*, 104678.
(38) Tanushi, X.; Pinna, G.; Vandamme, M.; Siberchicot, C.; D'Augustin, O.; Di Guilmi, A.-M.; Radicella, J. P.; Castaing, B.; Smith, R.; Huet, S.; Leteurtre, F.; Campalans, A. OGG1 Competitive Inhibitors Show Important Off-Target Effects by Directly Inhibiting Efflux Pumps and Disturbing Mitotic Progression. *Front. Cell Dev. Biol.* **2023**, *11*, 1124960.
(39) Cabral, J. E.; Lackner, A.; Jiang, W.; Lin, S.; Zhou, H.; Wu, A.; Demos, C.; Pham, M. A.; McNulty, R. NLRP10 Engages Oxidized DNA through a Schiff-Base Mechanism and Dissociates from NLRP3 upon Inflammasome Activation. *Commun. Biol.* **2026**, *9* (1), 72.
(40) Baquero, J. M.; Benítez-Buelga, C.; Rajagopal, V.; Zhenjun, Z.; Torres-Ruiz, R.; Müller, S.; Hanna, B. M. F.; Loseva, O.; Wallner, O.; Michel, M.; Rodríguez-Perales, S.; Gad, H.; Visnes, T.; Helleday, T.; Benítez, J.; Osorio, A. Small Molecule Inhibitor of OGG1 Blocks Oxidative DNA Damage Repair at Telomeres and Potentiates Methotrexate Anticancer Effects. *Sci. Rep.* **2021**, *11* (1), 3490.
(41) Pao, P.-C.; Patnaik, D.; Watson, L. A.; Gao, F.; Pan, L.; Wang, J.; Adaikkan, C.; Penney, J.; Cam, H. P.; Huang, W.-C.; Pantano, L.; Lee, A.; Nott, A.; Phan, T. X.; Gjoneska, E.; Elmsaouri, S.; Haggarty, S. J.; Tsai, L.-H. HDAC1 Modulates OGG1-Initiated Oxidative DNA Damage Repair in the Aging Brain and Alzheimer's Disease. *Nat. Commun.* **2020**, *11* (1), 2484.
(42) Xie, N.; Zhang, L.; Gao, W.; Huang, C.; Huber, P. E.; Zhou, X.; Li, C.; Shen, G.; Zou, B. NAD+ Metabolism: Pathophysiologic Mechanisms and Therapeutic Potential. *Sig Transduct Target Ther* **2020**, *5* (1), 227.
(43) Gardell, S. J.; Hopf, M.; Khan, A.; Dispagna, M.; Hampton Sessions, E.; Falter, R.; Kapoor, N.; Brooks, J.; Culver, J.; Petucci, C.; Ma, C.-T.; Cohen, S. E.; Tanaka, J.; Burgos, E. S.; Hirschi, J. S.; Smith, S. R.; Sergienko, E.; Pinkerton, A. B. Boosting NAD + with a Small Molecule That Activates NAMPT. *Nat. Commun.* **2019**, *10* (1), 3241.
(44) Murshudov, G. N.; Skubák, P.; Lebedev, A. A.; Pannu, N. S.; Steiner, R. A.; Nicholls, R. A.; Winn, M. D.; Long, F.; Vagin, A. A. REFMAC5 for the Refinement of Macromolecular Crystal Structures. *Acta Cryst D* **2011**, *67* (4), 355−367.
(45) Evans, P. Scaling and Assessment of Data Quality. *Acta Crystallogr D Biol Crystallogr* **2006**, *62* (1), 72−82.
(46) Collaborative Computational Project, Number 4 The CCP4 Suite: Programs for Protein Crystallography. *Acta Crystallogr D Biol Crystallogr* **1994**, *50* (5), 760−763.
(47) Emsley, P.; Cowtan, K. Coot: Model-Building Tools for Molecular Graphics. *Acta Crystallogr D Biol Crystallogr* **2004**, *60* (12), 2126−2132.
(48) Murshudov, G. N.; Skubák, P.; Lebedev, A. A.; Pannu, N. S.; Steiner, R. A.; Nicholls, R. A.; Winn, M. D.; Long, F.; Vagin, A. A. REFMAC5 for the Refinement of Macromolecular Crystal Structures. *Acta Cryst D* **2011**, *67* (4), 355−367.
(49) Krämer, A.; Kurz, C. G.; Berger, B.-T.; Celik, I. E.; Tjaden, A.; Greco, F. A.; Knapp, S.; Hanke, T. Optimization of Pyrazolo[1,5-a] Pyrimidines Lead to the Identification of a Highly Selective Casein Kinase 2 Inhibitor. *Eur. J. Med. Chem.* **2020**, *208*, 112770.

Downloaded from pubs.acs.org/jmcmar/article-pdf/69/20/23517/6749327/jm6c00526.pdf by UNIV OF SHEFFIELD user on 10 November 2026

(50) Fedorov, O.; Niesen, F. H.; Knapp, S. Kinase Inhibitor Selectivity Profiling Using Differential Scanning Fluorimetry. *Methods Mol Biol* **2012**, *795*, 109−118.
(51) Page, B. D. G.; Valerie, N. C. K.; Wright, R. H. G.; Wallner, O.; Isaksson, R.; Carter, M.; Rudd, S. G.; Loseva, O.; Jemth, A.-S.; Almlöf, I.; Font-Mateu, J.; Llona-Minguez, S.; Baranczewski, P.; Jeppsson, F.; Homan, E.; Almqvist, H.; Axelsson, H.; Regmi, S.; Gustavsson, A.-L.; Lundbäck, T.; Scobie, M.; Strömberg, K.; Stenmark, P.; Beato, M.; Helleday, T. Targeted NUDT5 Inhibitors Block Hormone Signaling in Breast Cancer Cells. *Nat. Commun.* **2018**, *9* (1), 250.
(52) Zhang, S. M.; Desroses, M.; Hagenkort, A.; Valerie, N. C. K.; Rehling, D.; Carter, M.; Wallner, O.; Koolmeister, T.; Throup, A.; Jemth, A.-S.; Almlöf, I.; Loseva, O.; Lundbäck, T.; Axelsson, H.; Regmi, S.; Sarno, A.; Krämer, A.; Pudelko, L.; Bräutigam, L.; Rasti, A.; Göttmann, M.; Wiita, E.; Kutzner, J.; Schaller, T.; Kalderén, C.; Cázares-Körner, A.; Page, B. D. G.; Krimpenfort, R.; Eshtad, S.; Altun, M.; Rudd, S. G.; Knapp, S.; Scobie, M.; Homan, E. J.; Berglund, U. W.; Stenmark, P.; Helleday, T. Development of a Chemical Probe against NUDT15. *Nat. Chem. Biol.* **2020**, *16* (10), 1120−1128.
(53) Michel, M.; Homan, E. J.; Wiita, E.; Pedersen, K.; Almlöf, I.; Gustavsson, A.-L.; Lundbäck, T.; Helleday, T.; Warpman Berglund, U. In Silico Druggability Assessment of the NUDIX Hydrolase Protein Family as a Workflow for Target Prioritization. *Front. Chem.* **2020**, *8*, 443.

Downloaded from pubs.acs.org/jmcmar/article-pdf/69/20/23517/6874932 7/jm6c00526.pdf by UNIV OF SHEFFIELD user on 10 November 2026

https://doi.org/10.1021/acs.jmedchem.6c00526
J. Med. Chem. 2026, 69, 23517−23539